OPTICS

The role of altered lipid composition and distribution in liver fibrosis revealed by multimodal nonlinear optical microscopy

Hao Jia[1]†, Juan Liu[2,3]†, Tinghe Fang[1], Zhen Zhou[1], Ruihong Li[2,3], Wenzhen Yin[4], Yao Qian[5], Qi Wang[2,3], Wanhui Zhou[1], Chang Liu[1], Dingcheng Sun[1], Xun Chen[1], Zheng Ouyang[5], Jiahong Dong[2,3], Yunfang Wang[2,3,4]*, Shuhua Yue[1]*

Intracellular lipid accumulation is commonly seen in fibrotic livers, but its exact role in liver fibrosis remains elusive. Here, we established a multimodal nonlinear optical microscopy to quantitatively map distribution of biomolecules in fibrotic livers. Our data revealed that unsaturated triglycerides were predominantly accumulated in central vein area during liver fibrosis but not in portal vein area. Moreover, the lipid homeostasis was remarkably dysregulated in the late-stage compared to the early-stage fibrosis, including increased unsaturated triglycerides with decreased lipid unsaturation degree and decreased membrane fluidity. Such alterations were likely due to up-regulated lipogenesis, desaturation, and peroxidation, which consequently led to endoplasmic reticulum stress and cell death. Inspiringly, injured hepatocyte could be rescued by remodeling lipid homeostasis via either supply of unsaturated fatty acids or enhancement of membrane fluidity. Collectively, our study improves current understanding of the role of lipid homeostasis in fibrosis and open opportunities for treatment.

INTRODUCTION

Liver is a highly dynamic and heterogeneous organ composed of the functional structural unit, the lobule (*1*). Blood flow along the lobule axis creates gradients of oxygen, nutrients, and hormones, known as zonation, which divides the lobule into central vein (CV), middle lobule, and portal vein (PV) areas (*2*, *3*). Liver pathologies often exhibit zonal patterns of phenotypic transformation with heterogeneous distribution of essential biomolecules. Thus, it is critical to depict a molecular landscape of tissue microenvironment for better understanding of liver disease progression.

Recurrent liver injury leads to liver inflammation and fibrosis, even severe cirrhosis and hepatocellular carcinoma (*4*, *5*). Excessive deposition of extracellular collagen fiber is considered to be a hallmark of liver fibrosis (*5*). On the basis of intrinsic signals from collagen crosslinking, second-harmonic generation (SHG) microscopy, one of the label-free nonlinear optical (NLO) imaging modalities, has been frequently used to quantitatively characterize collagen fiber deposition in liver fibrosis (*6*–*9*). Recently, the zonal distributions of collagen fibers and dominant pathogenic collagen-producing cells in fibrotic liver were uncovered (*10*, *11*).

Besides extracellular matrix, intracellular neutral lipid accumulation plays a crucial role in the maintenance of lipid metabolism for liver function. As a dynamic organelle for the storage of neutral lipids, lipid droplet (LD) predominantly stores triglycerides (TGs) and cholesteryl esters. Aberrant TG accumulation in LDs was commonly seen in various liver pathologies, such as hepatic steatosis and fatty liver diseases (*12*, *13*). Specifically, lipid accumulation in hepatocytes was found to induce fibrogenic activation of hepatic stellate cells (*14*). Nevertheless, the role of LD accumulation, including its chemical composition and zonal distribution, in pathological development and progression of liver fibrosis remains elusive.

Traditionally, LDs are visualized by specific staining, which lack compositional information (*15*). For analysis of lipid composition, mass spectrometry and nuclear magnetic resonance spectroscopy are commonly used but lack spatial information. Mass spectrometry imaging has been invented to map the spatial distribution of biomolecules but could hardly achieve subcellular resolution (*16*). Together, these methods mentioned above cannot provide the information regarding LD distribution and composition at the same time in intact tissue in situ, which hinders the study of LD biology in liver fibrosis.

Owing to the label-free detection capability, high molecular selectivity, and submicrometer spatial resolution, coherent Raman scattering (CRS) microscopy, one of the NLO imaging modalities, has shed new light on LD biology (*17*–*22*). As one type of CRS microscopy, coherent anti–Stokes Raman scattering (CARS) microscopy has been used to characterize hepatic fat in liver steatosis and fibrosis (*23*–*25*). However, because of nonresonant background, CARS microscopy has difficulties in quantitative analysis of LD composition. As another type of CRS microscopy, stimulated Raman scattering (SRS) microscopy can generate signals intrinsically free of nonresonant background and linearly proportional to the concentration of targeted biomolecules, which greatly facilitates

[1]Key Laboratory of Biomechanics and Mechanobiology (Beihang University), Ministry of Education, Institute of Medical Photonics, Beijing Advanced Innovation Center for Biomedical Engineering, School of Biological Science and Medical Engineering, Beihang University, Beijing 100191, China. [2]Hepato-Pancreato-Biliary Center, Beijing Tsinghua Changgung Hospital, Tsinghua University, Beijing 102218, China. [3]Research Unit of Precision Hepatobiliary Surgery Paradigm, Chinese Academy of Medical Sciences, Beijing, 102218, China. [4]Clinical Translational Science Center, Beijing Tsinghua Changgung Hospital, Tsinghua University, Beijing 102218, China. [5]State Key Laboratory of Precision Measurement Technology and Instruments, Department of Precision Instruments, Tsinghua University, Beijing 100084, China.
†These authors contributed equally to this work.
*Corresponding author. Email: yue_shuhua@buaa.edu.cn (S.Y.); wyfa02717@btch.edu.cn (Y.W.)

quantitative chemical imaging of lipids at the single cell level in situ (*18*, *26*–*29*). Recently, hyperspectral SRS microscopy was developed to quantitatively assess lipids in liver steatosis and hepatocellular carcinoma (*30*, *31*). Together, SRS microscopy could provide new insights into the role of lipid distribution and composition in liver fibrosis.

Here, we used label-free multimodal NLO microscopy, which integrated SHG imaging of collagen fibers, SRS imaging of TGs in LDs, and two-photon excited fluorescence (TPEF) imaging of autofluorescent metabolites in intact tissues on the same platform, to quantitatively map heterogeneous distribution of essential biomolecules in liver fibrosis at the single cell level. We first found the heterogeneous distribution of collagen fibers and TGs with different unsaturation degrees in the human liver tissues obtained at transplantation for liver injury or cirrhosis. Then, in the widely used chronic carbon tetrachloride (CCl_4)–induced mouse fibrosis model, it was found that as fibrosis progressed, TG accumulation was prominently increased in CV area along with collagen fiber deposition but almost absent in PV area. Compositional analysis showed that the total amount of unsaturated TGs significantly increased, but the lipid unsaturation degree significantly decreased in the late-stage compared to the early-stage fibrosis. Meanwhile, by mass spectrometry imaging, the unsaturation degree of membrane phospholipids was also found to significantly decrease as fibrosis progressed. Further, Laurdan staining indicated significantly increased membrane lipid order and decreased membrane fluidity in the late-stage fibrosis. To elucidate the mechanism by which altered lipid composition affects hepatocyte upon injury, we treated the human hepatic HepaRG cells with various types of fatty acids (FAs) and revealed that saturated FAs (SFAs) could remarkably induce LD accumulation with low unsaturation degree and solid-like membranes with high lipid order and low fluidity. On the basis of RNA sequencing (RNA-seq) data, such disrupted lipid and membrane homeostasis could lead to up-regulated endoplasmic reticulum (ER) stress and cell death, consistently with fibrotic tissues. We demonstrated that cellular processes of injured hepatocyte could be normalized by regulating lipid composition and membrane fluidity via either supply of protective unsaturated FAs (UFAs) or inhibition of SFAs delivery to membranes. Collectively, our work highlights the potential of multimodal NLO microscopy to uncover biological heterogeneity in liver diseases, elucidates the role of altered lipid composition and distribution in liver fibrosis, and offers a new way for liver fibrosis treatment.

RESULTS

Label-free quantitative imaging of TGs and collagen fibers in CV and PV areas during liver fibrosis by multimodal NLO microscopy

The TGs in LDs can be divided into saturated and unsaturated TGs. Considering the FA chains in TGs are predominantly oleate (C18:1) and linoleate (C18:2), we used glyceryl tristearate (TS) to represent saturated TGs, while we used glyceryl trioleate (TO) and glyceryl trilinoleate (TL) to represent unsaturated TGs (fig. S1, A to C). Among the unsaturated TGs, we designated the number of C═C on each FA chain as the lipid unsaturation degree. Specifically, the unsaturation degrees of TO and TL are 1 and 2, respectively.

First, we acquired the SRS spectra of TS, TO, and TL (Fig. 1A) and found that these three chemicals produced strong Raman characteristic peaks from 2800 to 3050 cm^{-1}, which was commonly described as CH region. The corresponding spontaneous Raman spectra were shown in fig. S1D. Specifically, we found that all the chemicals exhibited distinctive peaks at 2850 cm^{-1} corresponding to the CH_2 band. TO and TL exhibited a unique peak at 3010 cm^{-1} corresponding to ═C─H band for unsaturated TGs, while TS did not. As shown in Fig. 1B, SRS imaging of the three chemicals were performed by matching with the CH_2 and ═C─H bands. Bright-field signals were also taken at the same time (Fig. 1B). To quantify the lipid unsaturation degree, seven groups of mixed TG emulsions containing different concentration ratios of TO and TL were imaged by SRS microscopy (fig. S2A). We found that the SRS intensity ratio between the ═C─H band and the CH_2 band ($I_{=C-H}/I_{CH_2}$) was linearly proportional to the lipid unsaturation degree (Fig. 1C). Meanwhile, we also demonstrated that SHG can be used to visualize collagen fibers on the same microscope (fig. S2B).

Next, we performed spontaneous Raman spectral analysis of individual LDs accumulated in liver fibrotic tissues. As shown in fig. S3A, the spectra of intracellular LDs were nearly identical to the spectrum of pure chemicals, with characteristic bands of CH_2 bending mode at 1442 cm^{-1}, ester C═O band at 1745 cm^{-1}, and CH_2 symmetric stretching band at 2850 cm^{-1}. Unsaturated TGs showed prominent C═C band at 1655 cm^{-1} and ═C─H band at 3010 cm^{-1}. The autofluorescent granules in fibrotic tissues showed bands for lipid (1200 to 1800 cm^{-1}), amide I band at 1655 cm^{-1}, phenylalanine at 1000 cm^{-1}, and CH_3 symmetric stretching band of protein at 2930 cm^{-1} but lacked the characteristic ester C═O band at 1745 cm^{-1}. The corresponding assignments of Raman peaks are listed in table S1 (*32*–*34*). As shown in fig. S3 (B and C), the SRS spectra of individual LDs in CH region were also obtained.

Then, we performed multimodal NLO imaging of fibrotic liver tissue slices. Pairs of neighboring slices were sectioned, with one slice stained with hematoxylin and eosin (H&E) and the other remained unstained for multimodal NLO imaging (Fig. 1D). Morphologically, the SRS images provided information almost identical to that from the adjacent slices stained with H&E, which could identify the lobule with the same location. By tuning the laser wavelength to be resonant with CH_2 band at 2850 cm^{-1}, substantial SRS signals arose from lipid-rich cell membranes and intracellular LDs, whereas weak SRS signals were derived from lipid-poor cell nuclei (Fig. 1E and fig. S4). By tuning the laser wavelength to be resonant with ═C─H band at 3010 cm^{-1}, SRS signal of lipid membrane became more intense relatively to that taken from the CH_2 band at 2850 cm^{-1} (Fig. 1E and fig. S4). As shown in figs. S5 and S6, we used the SRS image of CH_2 band to extract total TGs and the SRS image of ═C─H band to extract unsaturated TGs. Subtracting the amount of unsaturated TGs from the amount of total TGs resulted in the amount of the saturated TGs. Furthermore, lipid unsaturation degree of the unsaturated TGs was quantified on the basis of the calibration curve shown in Fig. 1C. Meanwhile, by integrating SHG on the same microscope, the zonal distribution of collagen fibers was observed across the lobule. As shown in the merged image in Fig. 1E, the collagen fiber deposition and TG accumulation were notably higher in CV area than that in PV area, and they occurred accompanied with each other. These data together demonstrated that multimodal NLO imaging could reveal molecular zonation of extracellular collagen fibers and intracellular lipids in unstained fibrotic tissue in situ.

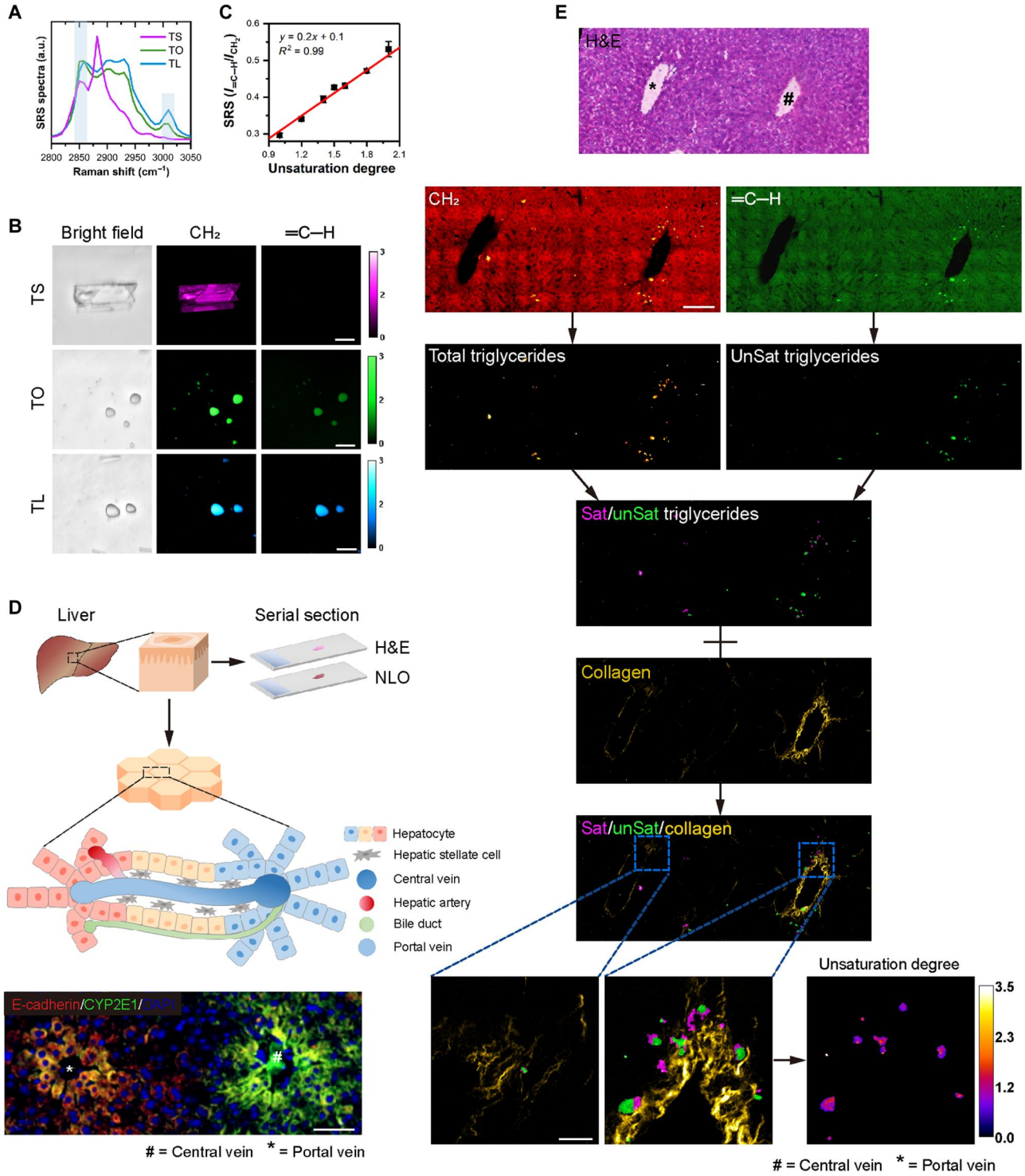

Fig. 1. Label-free quantitative multimodal NLO imaging of TGs and collagen fibers in pure chemicals and fibrotic liver tissues. (**A**) SRS spectra of TS, TO, and TL in CH vibrational region. a.u., arbitrary units. (**B**) SRS and bright-field imaging of TS, TO, and TL at CH_2 band (2850 cm^{-1}) and =C—H band (3010 cm^{-1}), respectively. Scale bars, 20 μm. (**C**) Calibration curve of lipid unsaturation quantification. SRS intensity ratio $I_{=C-H}/I_{CH_2}$ = 0.2 × unsaturation degree + 0.1. Error bars represent SD (n = 3). (**D**) Liver tissue sectioning process and the zonation of liver lobule. Immunofluorescence of CV marker Cyp2e1 (green color) and PV marker E-cadherin (red color). Cell nuclei were stained by DAPI (blue color). Scale bar, 50 μm. (**E**) Multimodal NLO imaging of CV and PV area in intact liver tissue. Saturated (Sat) TGs, unsaturated (unSat) TGs, collagen fibers and lipid unsaturation degree are shown in magenta, green, yellow, and fire colors, respectively. Blue dashed lines mark magnified areas. Scale bar in large-scale images, 50 μm. Scale bar in magnified images, 20 μm. H&E, hematoxylin and eosin.

Heterogeneous distribution of collagen fibers and TGs with different unsaturation degree in human pathological liver tissues

By using the multimodal NLO microscopy, we quantitatively mapped the distribution of collagen fibers and different types of lipids simultaneously in the human liver tissue specimens obtained at transplantation for liver injury or cirrhosis (table S2). Although the zonal difference between CV and PV areas in the cirrhosis specimens became less pronounced, with partial to complete loss of zonation and lobular structure, we still found a heterogeneous distribution of lipids and collagen fibers. As shown in Fig. 2 and figs. S7 to S10, the vessel-like structures were surrounded by abundant collagen fibers and lipids. The lipid components, including saturated/unsaturated TGs and lipofuscins, which are autofluorescent lipid peroxidation products, were heterogeneously distributed (Fig. 2F). It should be noted that lipid accumulation seemed to occur accompanied with the collagen fiber deposition. However, the molecular distribution was heterogeneous among different specimens, probably due to the different stage of disease progression for each patient. These results suggest that the zonal patterns

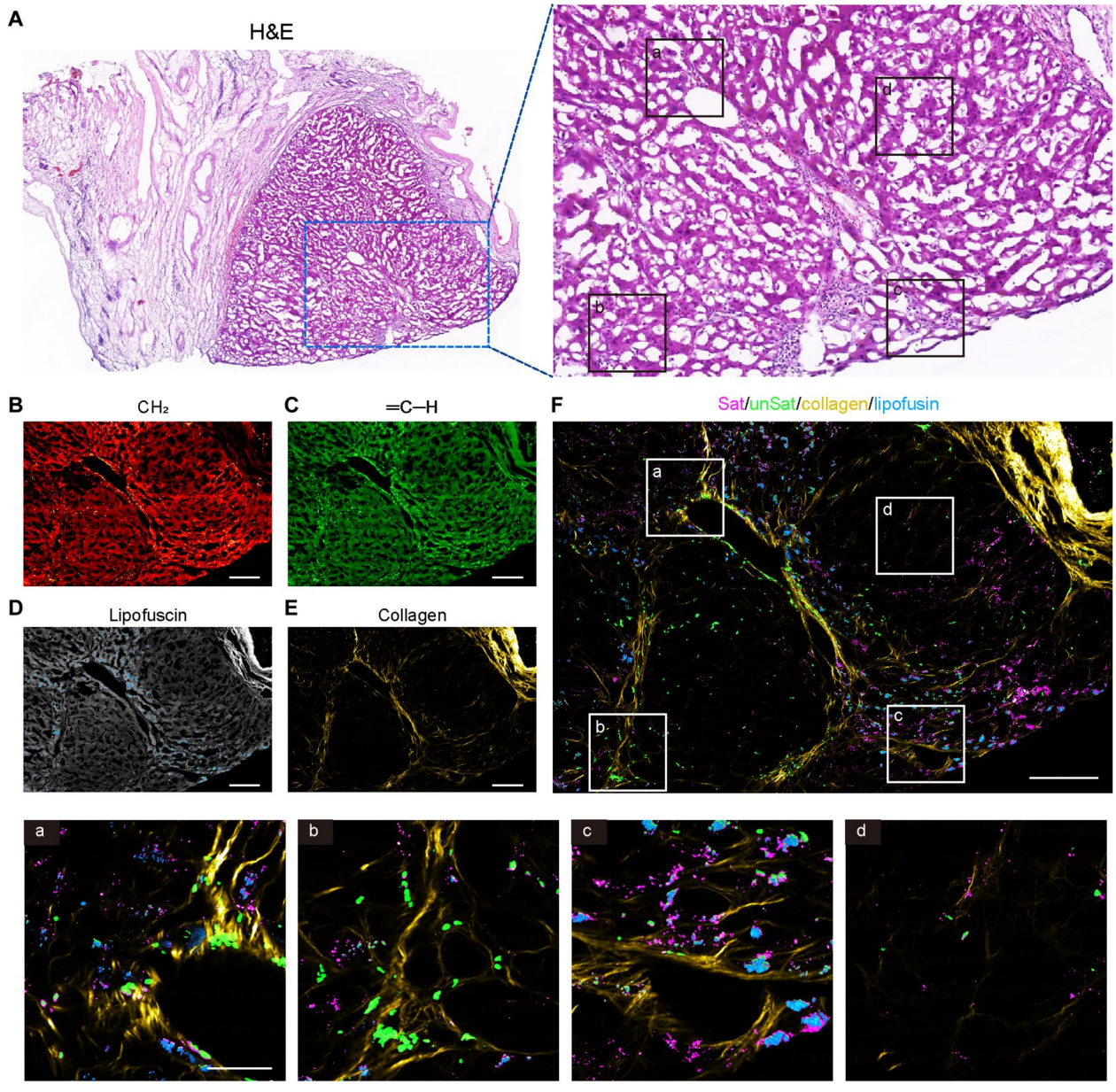

Fig. 2. Heterogeneous distribution of lipids and collagen fibers in human liver tissues. (**A**) H&E image of human liver samples from patient no.1. The magnified area indicates the imaging region of adjacent slice. (a) to (d) represent different regions of interest. (**B**) SRS imaging of the CH_2 band (red color). Scale bar, 200 μm. (**C**) SRS imaging of the =C—H band (green color). Scale bar, 200 μm. (**D**) TPEF imaging of the autofluorescent granules, lipofuscin (cyan color). Scale bar, 200 μm. (**E**) SHG imaging of the collagen fibers (yellow color). Scale bar, 200 μm. (**F**) The merge image of Sat TGs (magenta color), unSat TGs (green color), lipofuscin (cyan color), and collagen fibers (yellow color) in human liver tissue. Scale bar, 200 μm. (a) to (d) represent different regions of interest. Scale bar, 50 μm.

of collagen fibers and lipids may be potential biomarkers to assess liver fibrosis progression.

Alteration in TG distribution during liver fibrosis

To investigate the zonal distribution of TGs during fibrosis development, a widely used CCl_4-induced mouse centrilobular fibrosis model that could reproduce major characteristics of human liver fibrosis (*35*–*37*) was established. Liver tissues harvested from CCl_4-treated mice at specific time points on weeks 0, 2, 4, 6, 8, and 12 were analyzed (Fig. 3A and fig. S11). All lobule examinations were confirmed by the H&E sections (fig. S12A). Representative multimodal NLO images were shown in Fig. 3B and fig. S12B. The magnified images (Fig. 3B) showed that the accumulations of both collagen fibers and TGs were accompanied with each other. Quantitative analysis showed that collagen fiber deposition in CV area increased rapidly and significantly as the fibrosis progressed (Fig. 3C). At week 12, the amount of collagen fiber was found to be ~15%, significantly higher by ~5-fold compared to the control group. In PV area, the deposition of collagen fiber did not increase significantly until week 12 (Fig. 3C). From week 6, the amount of collagen fibers in CV area was significantly greater than that of PV area at various time points of fibrosis (table S3). Along with collagen fiber deposition, TG amount in CV area also accelerated significantly and even reached by ~14-fold in week 12 compared to the control group, while almost absent in PV area (Fig. 3C). There were also obvious differences between CV and PV areas at various time points of fibrosis from week 2 (table S4). These data collectively revealed a hidden signature of liver fibrosis, that is, zonal pattern of TG accumulation in fibrotic liver, which suggests that molecular zonation of TGs is closely associated with the development and progression of liver fibrosis.

Alteration in TG composition during liver fibrosis

Not only the distribution but also the composition of TGs was found to change during fibrosis. The proportion of unsaturated TGs in CV area significantly increased as fibrosis progressed (Fig. 3D and table S5). Specifically, there were ~97% saturated TGs at week 0, which almost all converted to unsaturated TGs at week 12 (~94%). Because the amount of TGs in PV area was very limited, the composition of TG in PV area was not further analyzed. Together, the amount of TGs, more specifically unsaturated TGs, significantly increased in CV area during fibrosis but not in PV area, suggesting that the zonated lipid unsaturation is closely associated with fibrosis development.

Within the unsaturated TGs in CV area, we then sought to elucidate how exactly the lipid unsaturation degree changed as fibrosis progressed. According to the established method in Fig. 1, the lipid unsaturation degree was quantitatively mapped in the fibrotic tissues (Fig. 4A). Because of the very low amount of unsaturated TG, the lipid unsaturation degree was not analyzed in the control group. Our data found that the lipid unsaturation degree showed a relatively high level of ~2 at weeks 2 and 4, and decreased to the level of ~0.5 at week 6 and thereafter (Fig. 4B). To explore why the unsaturation degree changed, we quantitatively analyzed composition of individual LDs. It was found that most of the LDs had lipid unsaturation degree above 1 at weeks 2 and 4, and a new population appeared with lipid unsaturation degree lower than 1 from weeks 6 to 12 (Fig. 4, C and D). We speculated that the emergence of such new population might be due to greater proportion of SFA chains relative to UFA chains, which were responsible for the decreased lipid unsaturation degree in the late-stage liver fibrosis. Along with the decreased lipid unsaturation degree in CV area, we also found some intracellular autofluorescent granules from week 2, which were probably lipofuscins, lipid peroxidation products (Fig. 4E). Quantitative analysis showed that lipofuscin accumulation in CV area significantly increased and reached by ~4-fold in week 12 compared to week 2 of fibrosis (Fig. 4F). Together, our data suggest that the alteration of TG composition might play an important role in liver fibrosis.

Next, we conducted the gene ontology (GO) analysis of three public transcriptomic datasets [available in Gene Expression Omnibus (GEO) with the accession IDs GSE214119, GSE207855, and GSE205540 (*38*)] at different stages of CCl_4-induced liver fibrosis. As shown in fig. S13, the genes related to FA desaturation, including stearoyl–coenzyme A (CoA) desaturase 2 and FA desaturase 3, were significantly up-regulated in fibrotic liver. Furthermore, since polyunsaturated FAs (PUFAs) were considered to be the major substrates for lipid peroxidation, we hypothesized that the increased lipofuscinogenesis might be due to the increased lipid peroxidation in the late-stage fibrosis. To test this hypothesis, we performed immunohistochemistry (IHC) on malondialdehyde (MDA), a secondary product of lipid peroxidation and found an evident increase of MDA accumulation, which was significantly more prominent in CV area than that in PV area, in the late-stage fibrosis (fig. S14). The GO analysis also indicated up-regulation of the genes related to oxidative stress (e.g., transforming growth factor-β). Together, our data imply that lipid desaturation and lipid peroxidation are very likely to promote liver fibrosis.

Association of TG composition with phospholipid composition and membrane fluidity that consequently links to ER stress in liver fibrosis

Considering LDs are involved in the maintenance of membrane homeostasis (*39*), we speculated that membrane lipid composition could be changed along with the altered TG composition during liver fibrosis. To test the hypothesis, we conducted mass spectrometry imaging of phosphatidylcholines (PCs), which account for >50% of the phospholipids in most eukaryotic membranes. Quantitative analysis showed that the unsaturation degree of PCs significantly decreased as fibrosis progressed (fig. S15, Fig. 5A, and table S6), which was consistent with the alteration in TG composition. Specifically, at week 12, the proportion of low unsaturation degree (<2) in PCs was found to be ~75%, significantly higher by ~3-fold compared to the early-stage fibrosis.

To find out how the compositional changes of TGs could influence membrane phospholipid composition, we performed IHC on liver FA binding protein 1 (FABP1), a lipid "chaperone" known to regulate mobility of FAs and have higher affinity to SFAs compared to UFAs (*40*, *41*). As shown in Fig. 5B, FABP1 was up-regulated during fibrosis, which might promote efficient delivery of FAs with lower unsaturation degree to the membrane and further change phospholipid composition.

Lipid composition has been shown to affect physical phase of lipids on cellular membranes in various disease (*42*). Lipid domains in different phase states have different packing and fluidity. For example, lipids with low unsaturation degree result in the ordered phase, which makes lipids tight packing and membranes less fluid (*43*, *44*). To address whether the alteration of membrane

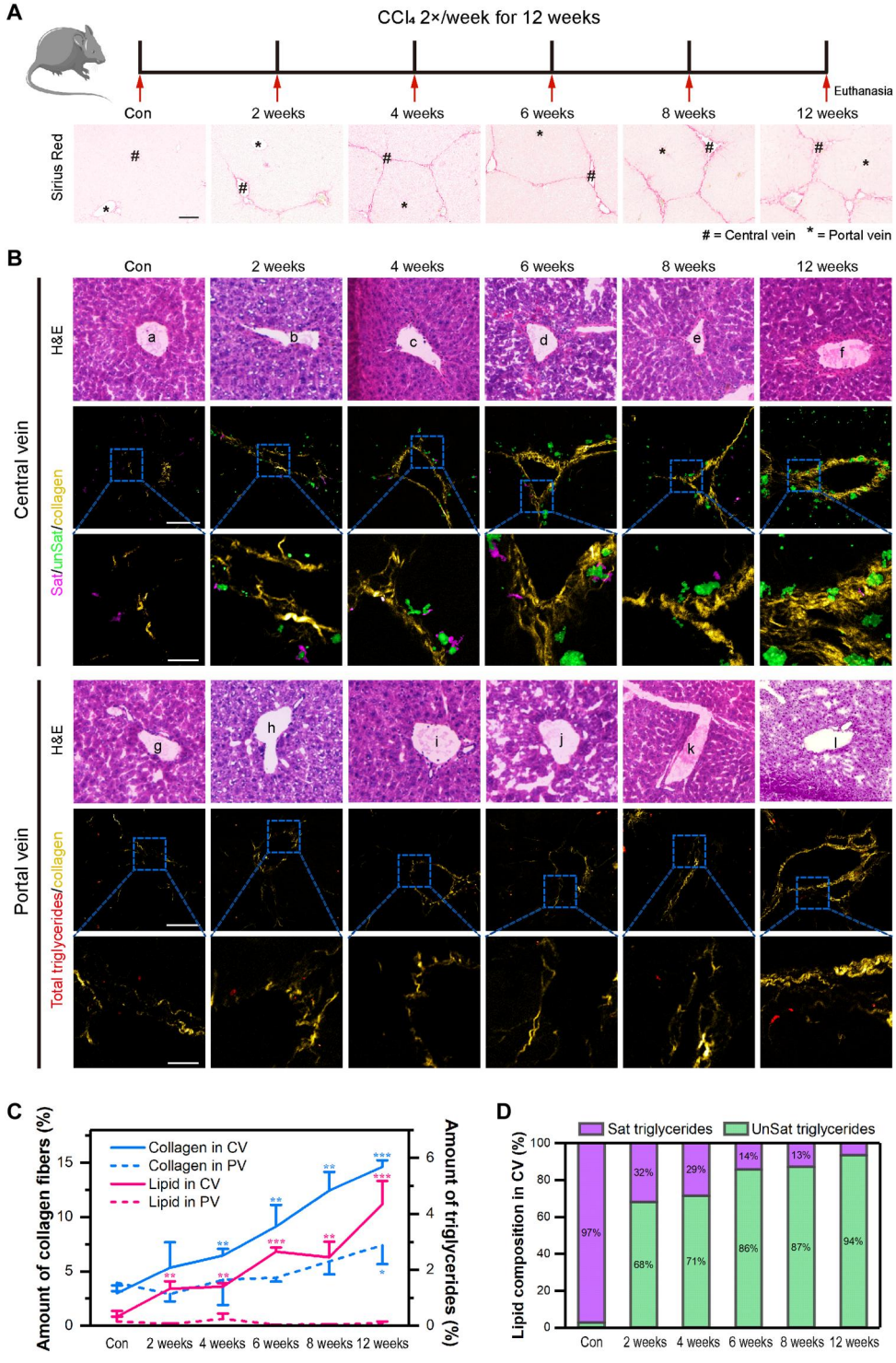

Fig. 3. Multimodal NLO imaging of TGs and collagen fibers in CV and PV areas of mouse fibrotic liver tissues. (**A**) CCl_4-induced liver injury mouse model (top). Sirius Red staining images of liver tissue sections at various time points in CCl_4 fibrosis model (bottom). Scale bar, 100 μm. (**B**) The multimodal NLO images of total TGs (red color), Sat TGs (magenta color), unSat TGs (green color), and collagen fibers (yellow color) in mouse fibrotic liver tissues. The corresponding H&E images of the neighboring slices were also shown. Top, CV area; bottom, PV area. Scale bars in large-scale images, 100 μm. Scale bars in magnified images, 20 μm. (**C**) Quantitative analysis of TG amount and collagen fiber amount in CV and PV areas at various time points. Error bars represent SD. The Student's *t* test, $^{*}P < 0.05$, $^{**}P < 0.01$, and $^{***}P < 0.001$. (**D**) The TG composition in CV area, including Sat and unSat TGs.

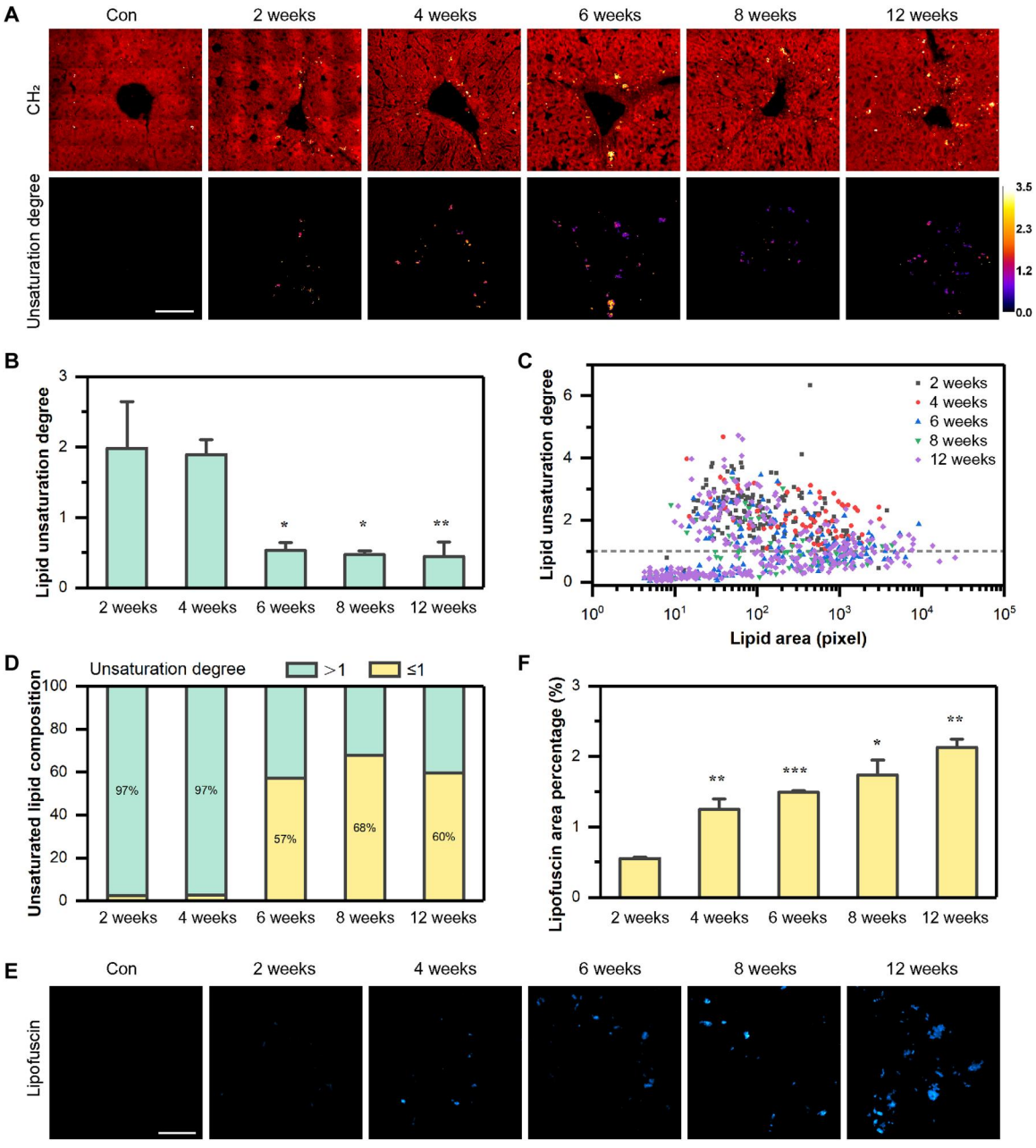

Fig. 4. Lipid desaturation and peroxidation in CV area during fibrosis. (**A**) SRS imaging (CH_2 band at 2850 cm^{-1}) of CV area (top, red color) and the quantitative mapping of lipid unsaturation degree (bottom, fire color) at various time points of fibrosis. Scale bar, 100 μm. (**B**) Quantification of lipid unsaturation degree at various time points. Error bars represent SD. The Student's *t* test, $^*P < 0.05$ and $^{**}P < 0.01$. (**C**) Correlation analysis of LD size and lipid unsaturation degree. The gray dashed line indicates the unsaturation degree of 1. (**D**) The lipid unsaturation degree of LDs in CV area at various time points. Cyan color, unsaturation degree > 1; yellow color, unsaturation degree ≤ 1. (**E**) TPEF imaging of the autofluorescent granules, lipofuscin (cyan color). Scale bar, 50 μm. (**F**) Quantification of lipofuscin at various time points. Error bars represent SD. The Student's *t* test, $^*P < 0.05$, $^{**}P < 0.01$, and $^{***}P < 0.001$.

lipid composition could affect lipid order and membrane fluidity during fibrosis, we conducted 6-lauryl-2-dimethylamino-naphthalene (Laurdan) staining on fibrotic liver tissues. Laurdan, a polarity-sensitive membrane probe, can provide a quantitative readout of the relative order of the lipids based on shifts in the emission spectra profiles generated by probe binding to ordered versus disordered phases of the membrane (*45*, *46*). Laurdan staining has been widely used for quantitative assessment of membrane lipid order in a variety of biological specimens (*45*, *46*). Specifically, the parameter called generalized polarization (GP) is a commonly used proxy for membrane physical properties, with higher values reporting higher lipid order and less membrane fluidity. As the GP images shown in Fig. 5C, the membrane lipid order of the liver tissue in late-stage fibrosis was higher than that in control and early-stage fibrosis. Statistical analysis of GP values further indicated

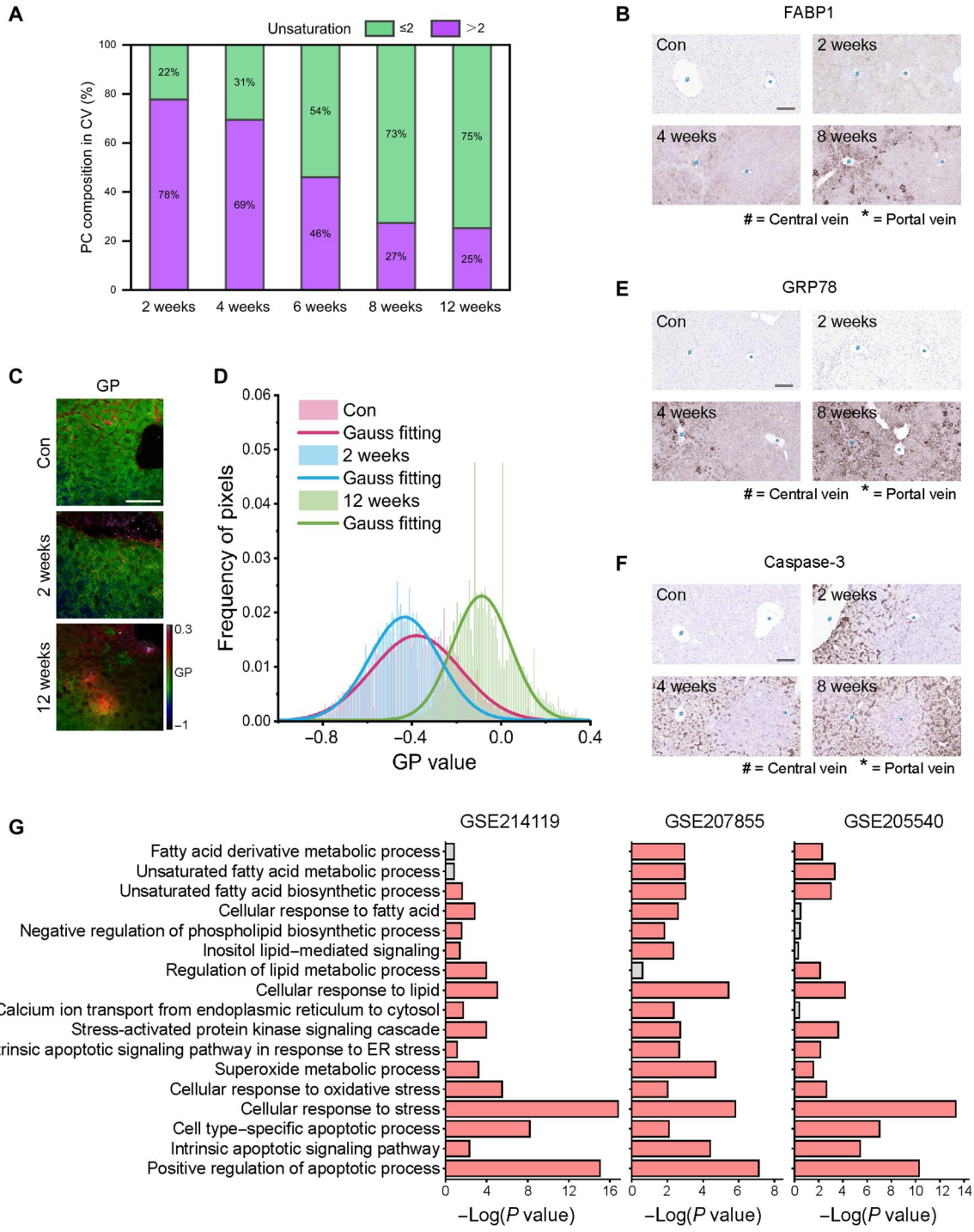

Fig. 5. The analysis of phospholipid composition, membrane fluidity, gene, and protein expressions in fibrotic liver tissues. (**A**) The composition of PC with different unsaturation degrees. (**B**) IHC of FABP1 at various time points of fibrosis (brown color). Scale bar, 100 μm. (**C**) Representative Laurdan images of membrane lipid order in fibrotic liver tissues at weeks 0, 2, and 12. Merged mean intensity and rainbow red-green-blue (RGB) pseudocolored generalized polarization (GP) images are shown. Red colors indicate high membrane order and less membrane fluidity, whereas blue colors indicate low membrane order and high membrane fluidity. Scale bar, 50 μm. (**D**) Distribution of the GP values in fibrotic liver tissues in (C). The histograms for fibrotic liver tissues at week 12 were shifted to high GP values. (**E**) IHC of GRP78 at various time points of fibrosis (brown color). Scale bar, 100 μm. (**F**) IHC of caspase-3 at various time points of fibrosis (brown color). Scale bar, 100 μm. (**G**) Reactome pathway–based gene set enrichment analysis showing pathways up-regulated at different time points of CCl_4-induced liver fibrosis from three public transcriptomic datasets. Accession IDs of GSE214119, GSE207855, and GSE205540 represent CCl_4-induced liver fibrosis at weeks 4, 6, and 8, respectively. Red colors indicate *P* value less than 0.05, whereas gray colors indicate *P* value greater than 0.05. caspase-3, cysteine-aspartic acid protease.

significantly increased lipid order and decreased membrane fluidity in the late-stage fibrosis (Fig. 5D).

Given that low lipid unsaturation degree and high membrane lipid order could induce ER stress (*47*, *48*), we next conducted IHC on 78-kDa glucose-regulated protein (GRP78), one of the ER stress markers, and found that GRP78 was up-regulated during fibrosis (Fig. 5E). Furthermore, since ER stress could induce cell apoptosis, we then performed IHC on cysteine-aspartic acid protease (caspase-3), a key enzyme of cell apoptosis, and found an evident increase of caspase-3 expression during fibrosis (Fig. 5F).

Furthermore, the GO analysis of three public transcriptomic datasets [available in GEO with the accession IDs GSE214119, GSE207855, and GSE205540 (*39*)] revealed extensive up-regulation of molecular pathways correlated with lipid metabolism, oxidative stress, ER stress, and cell apoptosis, in fibrotic liver compared to control liver (Fig. 5G and fig. S13). Specifically, up-regulated lipid metabolism pathways mainly included UFA biosynthetic process, phospholipid biosynthetic process, cellular response to FA, and superoxide metabolic process. These data were consistent with our multimodal NLO imaging, Laurdan staining, and IHC results. Together, these findings unravel the association of TG composition with phospholipid composition and membrane fluidity that consequently links to ER stress in liver fibrosis.

Induction of solid-like membrane and subsequent ER stress by SFA stimulus in hepatocyte

Liver fibrosis has been shown to promote de novo lipogenesis (*49*). To investigate which type of FAs contributes to the alteration of TG composition and membrane fluidity, we treated human hepatic cell line HepaRG with a panel of FAs of different unsaturation degree, including palmitate acid (PA; 16:0), oleic acid (OA; 18:1), and eicosapentaenoic acid (EPA; 20:5), to represent SFA, monounsaturated FA, and PUFA, respectively. In particular, for observation of newly synthesized lipids by PAs, we used deuterium-labeled PAs (PA-d_{31}), which exhibited distinctive peak for C─D band around 2107 cm^{-1}. Consistent with previous studies (*44*, *50*), we found that PAs promoted the formation of not only TGs in LDs but also solid-like membrane structures. These newly synthesized TGs in PA treatment group were nearly all saturated, and the solid-like membrane structures showed significantly higher membrane lipid order relative to the control group (Fig. 6, A and B). On the contrary, both OAs and EPAs incorporated into TGs rather than membrane lipids (fig. S16A). Quantitatively, the total TGs and unsaturated TGs were markedly increased after OA or EPA treatment compared to the control and PA treatment groups, and OA treatment group showed the greatest TG and unsaturated TG accumulation (fig. S16, B to D). The unsaturation degree of TGs in EPA treatment group was significantly higher than the OA treatment group (fig. S16E). Neither OAs nor EPAs altered the membrane lipid order compared to the control (fig. S16A). It needs to be mentioned that the red spot–like structures in GP images of cells treated with OAs and EPAs (fig. S16) were actually LDs, confirmed in fig. S17. In this work, we focused on the order of membrane lipids rather than LDs, so the GP values of LDs were excluded from the analysis. These results together indicate that the SFA stimulus could promote saturated TG accumulation in LDs and induce solid-like membranes with higher order and less fluidity in hepatocytes.

Next, to reveal the involved gene regulatory pathways, we carried out RNA-seq transcriptomic analysis on HepaRG cells treated with or without PAs. As shown in fig. S18C and Fig. 6C, for PA-treated cells compared to the control, the genes related to liver injury (FGF21 and MFSD2A) were up-regulated, while the genes related to cytoskeleton remodeling (MPDZ, RDX, and IQGAP1), cell adhesion (AMIGO2, FAT4, and TMOD3), DNA repair (MSH2), and cell cycle progression (CDK6, CCND1, BUB1B, and ECT2) were down-regulated. Notably, ER stress–related genes, such as ATF4, STC2, JUN, XBP1, DDIT3, CXCL8, and ATF3, and cell death–related genes, including CDKN1A, PMAIP1, BBC3, TRIB3, and GADD45A, were all up-regulated (Fig. 6C), consistent with the results in fibrotic tissues. In terms of lipid metabolism–related genes, it was found that the gene related to TG homeostasis (ANGPTL4) was up-regulated, while the genes related to membrane lipid organization (CAV1), calcium-dependent phospholipid binding (C2CD5), and transmembrane transporter activity (SLC26A2, SLC39A6, and SLC4A7) were down-regulated (Fig. 6C), in PA-treated cells.

Collectively, these data suggest that SFA treatment on hepatocyte may be an appropriate model to mimic the dysregulated lipid homeostasis in liver fibrotic tissues. SFA stimulus could induce dysregulation of lipid homeostasis in hepatocyte, which further leads to ER stress and cell death.

Normalization of lipid homeostasis and cellular processes in injured hepatocyte by regulating lipid composition and membrane fluidity

We lastly explored the impact of regulating TG composition and membrane fluidity on cellular processes in injured hepatocytes. We first supplied PA-treated hepatocytes with extra OAs or EPAs and found remarkable conversion from solid-like membrane structures to TGs (Fig. 7A). On the basis of Laurdan staining, GP values of the membrane lipids in the cotreatment groups (PA + OA and PA + EPA) were both significantly reduced compared to the PA alone group, suggesting that the PA-induced solid-like membrane with high lipid order could be normalized by UFAs in hepatocytes. Meanwhile, the amounts of TGs in PA + OA and PA + EPA groups were both significantly increased relative to the PA alone group (Fig. 7B), suggesting that UFAs could facilitate SFA incorporation into LDs to prevent from lipotoxicity in hepatocytes. For TG composition, both cotreatment groups were shown to significantly increase the amount of unsaturated TGs compared to the PA alone group (Fig. 7, C and D), and the lipid unsaturation degrees were also significantly higher in the cotreatment groups than the PA alone group (Fig. 7E).

Next, we tested whether lipid homeostasis can be normalized by suppressing the delivery of SFAs to membranes. We treated the SFA-injured hepatocytes with the inhibitor of FABP, BMS-309403 (BMS), and also observed evident increase of membrane fluidity and TG accumulation (Fig. 7A). The Laurdan staining images showed that cotreatment SFA with BMS (PA + BMS) significantly decreased the membrane lipid order compared to the PA alone group (Fig. 7A). Meanwhile, the amounts of TGs and unsaturated TGs and the lipid unsaturation degree in PA + BMS group were all significantly increased compared the PA alone group (Fig. 7, B to E). Notably, BMS alone did not alter the TG accumulation or membrane lipid order compared to the control group (fig. S16, A to E).

Last, we carried out RNA-seq transcriptomic analysis on the cells treated with PA alone, PA + OA, and PA + BMS (fig. S18). As shown in Fig. 7F, it was found that the genes related to lipid biosynthesis,

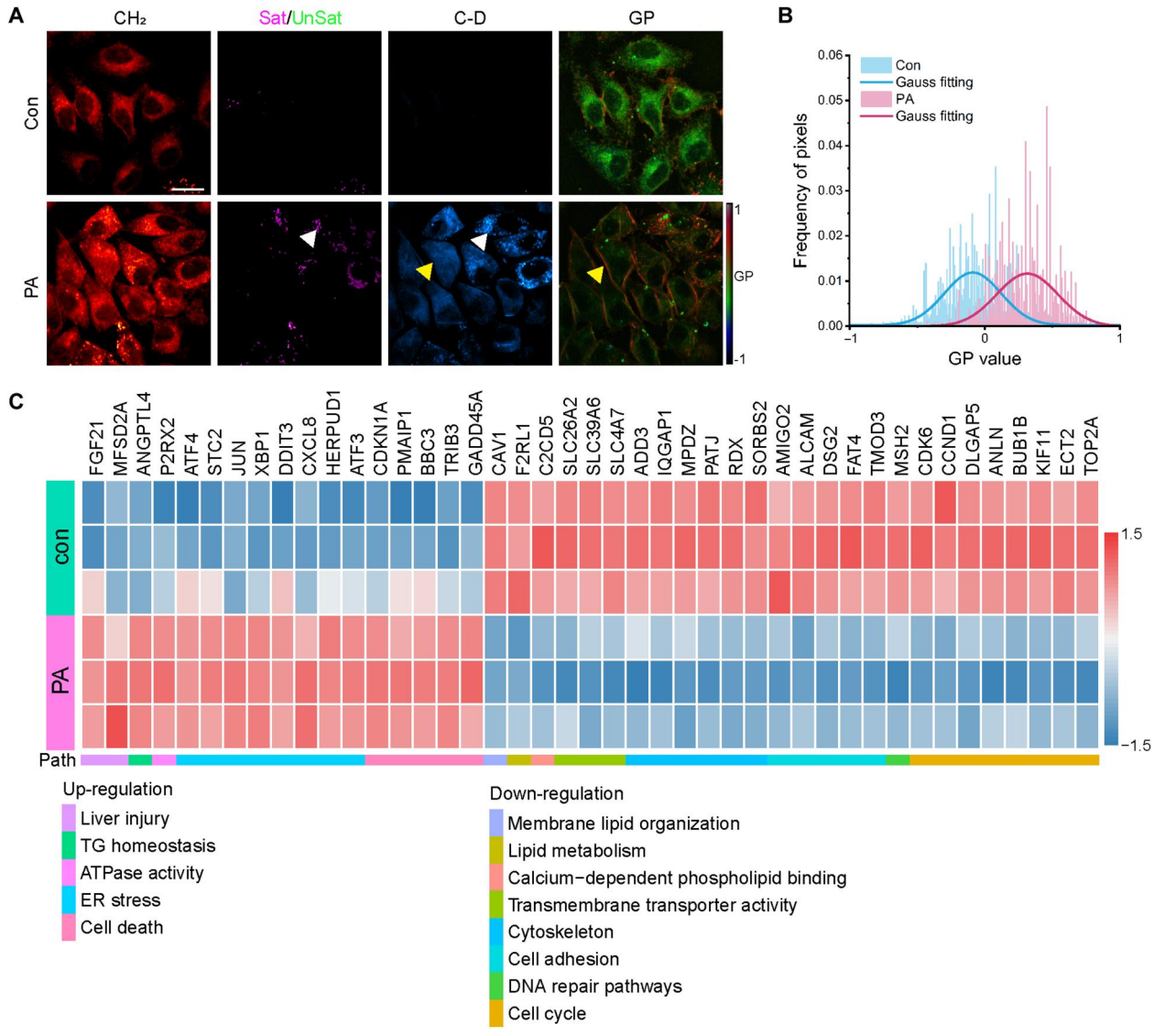

Fig. 6. The effects of PA stimulus on lipid homeostasis and cellular processes in hepatocytes. (**A**) The SRS images of Sat TGs (magenta color), unSat TGs (green color), newly synthesized TGs (cyan color), and Laurdan images (RGB pseudocolor) in HepaRG cells treated with or without PAs for 4 hours. In merged mean intensity and rainbow RGB pseudocolored GP images, red colors indicate high membrane order and less membrane fluidity, whereas blue colors indicate low membrane order and high membrane fluidity. White color arrowheads indicate newly synthesized LDs. Yellow color arrowheads indicate newly synthesized solid-like membrane structures. Scale bar, 20 μm. (**B**) Distribution of the GP values in cells treated with or without PAs. The histograms for PA-treated cells are shifted to high GP values. (**C**) Heatmap showing expression of differentially expressed genes in cells treated with or without PAs. ATPase, adenosine triphosphatase.

such as INSIG1, FASN, LDLR, and LRP1/5, were down-regulated in the PA + OA group, suggesting that the cells did not require much lipogenesis upon exogenous supplementation of UFAs. Moreover, the down-regulation of cellular apoptosis–related gene CASP2 indicated reduced cell death upon UFA supply. In terms of the PA + BMS group, the genes related to lipid modifying enzyme (SMPDL3B), transforming growth factor (GDF15), peroxidation (GPX1), and lipolysis (MGLL) were down-regulated (Fig. 7G). Several membrane lipid–related genes were up-regulated, for example, GPAT3 for TG synthesis, ATP8B1, LPGAT1, LPIN1, SELENOI, CPNE3, PIKFYVE, PLEKHA1, SNX2, and ITPR2 for glycerophospholipid metabolism, LPAR1 and LIPH for lysophosphatidic acid metabolism, and C2CD5, CEP97, and PLSCR4 for ion homeostasis. Furthermore, cytoskeleton remodeling (IQGAP1, MPDZ, and RDX)–, cell adhesion (CGNL1 and FER)–, and cell cycle progression (CDK6, CDC14A, CDC7, and CEP57)–related genes were also up-regulated (Fig. 7G) in the PA + BMS group. These transcriptomic findings support that UFA and BMS could normalize lipid homeostasis and cellular processes in injured hepatocyte by regulating lipid composition and membrane fluidity.

DISCUSSION

Through integrated analyses of injured liver tissues from patients, liver fibrotic tissues from mouse model, and cell line by multimodal

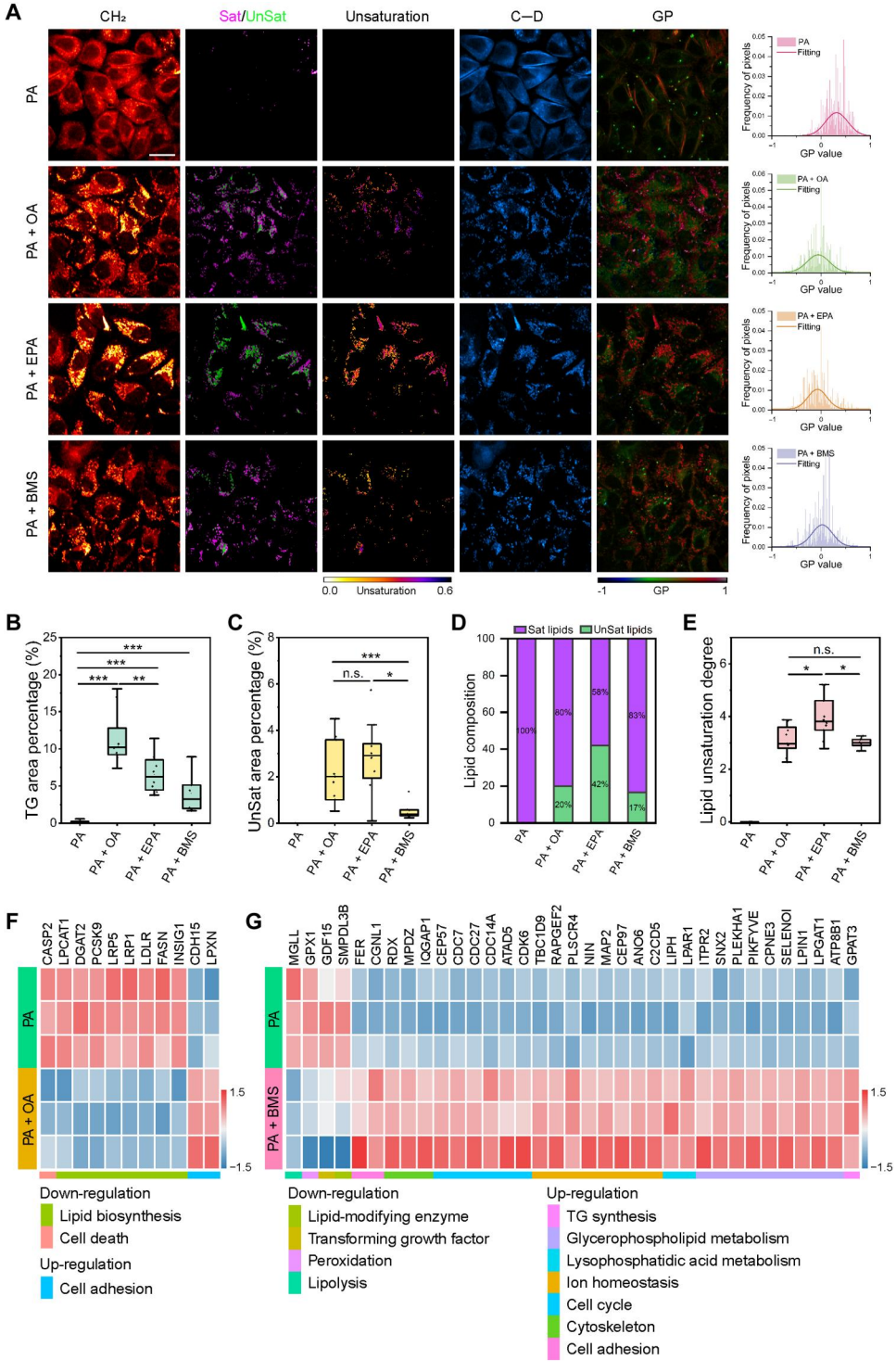

Fig. 7. The effect of UFA and FABP inhibitor BMS on lipid homeostasis and cellular processes in injured hepatocytes. (**A**) The SRS images of Sat TGs (magenta color), unSat TGs (green color), newly synthesized TGs (cyan color), and Laurdan images (RGB color) in HepaRG cells treated with PA, cotreated with OA and PA, cotreated with EPA and PA, and cotreated with BMS and PA. Cells in the groups of PA, PA + OA, and PA + EPA were treated for 4 hours. Cells in the group of PA + BMS were treated with BMS for 24 hours during concomitant incubation with PA for 4 hours. (**B**) Quantitative analysis of total TG amount. (**C**) Quantitative analysis of unsaturated TG amount. (**D**) Quantitative analysis of TG composition. (**E**) Quantitative analysis of lipid unsaturation degree. The Student's *t* test in (B) to (E), $^{*}P < 0.05$, $^{**}P < 0.01$, and $^{***}P < 0.001$. Error bars represent SD. (**F**) Heatmap showing expression of differentially expressed genes in cells treated with PA and cells treated with PA + OA. (**G**) Heatmap showing expression of differentially expressed genes in cells treated with PA and cells treated with PA + BMS. n.s., not significant.

NLO imaging, mass spectrometry imaging, Laurdan staining, IHC, and RNA-seq transcriptomics, we have revealed essential roles of altered lipid composition and distribution in liver fibrosis. LD accumulation is known to be a hallmark of various liver pathologies; however, the role of LD accumulation, including its chemical composition and zonal distribution, in liver fibrosis remains unknown. In this study, we found the heterogeneous accumulation of LDs, primarily composed of TGs, in CV area but not in PV area, along with collagen fiber deposition in liver fibrosis. The lipid composition was remarkably changed in the late-stage compared to the early-stage fibrosis, including the increased amount of unsaturated TGs, the decreased lipid unsaturation degree of both unsaturated TGs and phospholipids, and the increased membrane lipid order, which together dysregulated lipid and membrane homeostasis. Such alterations could be due to up-regulated lipogenesis, desaturation, transport, and peroxidation, which consequently led to ER stress and cell death. Further cellular studies revealed that SFA stimulus could induce LD accumulation with low unsaturation degree and solid-like membranes with high lipid order and low fluidity, consistent with fibrotic tissues. Inspiringly, the remodeling of lipid composition and membrane fluidity were capable to normalize cellular processes of injured hepatocyte by either supply of protective UFAs or enhancement of membrane fluidity. As discussed below, these findings improve current understanding of the role of lipid homeostasis in fibrosis and open opportunities for treatment of liver fibrosis.

First, our study offers a great platform to study heterogeneous distribution of biomolecules in situ at the single cell level. Liver zonation is considered to confer optimality for liver function, which plays an important role in liver physiology and pathology. Our work used a label-free multimodal NLO imaging platform, which integrated SRS, SHG, and TPEF, to study heterogeneous distribution of essential biomolecules, including TG, collagen fiber, and lipofuscin, in intact liver tissues. Such multimodal imaging platform could depict a molecular landscape of tissue microenvironment in situ without any processing or exogenous labeling, which allowed us to gain new insight into the development and progression of liver diseases. Few existing methodologies can provide quantitative visualization of both molecular amount and compositional information at the single-cell level noninvasively. We expected that this multimodal microscopy could facilitate the discovery of zonal patterns of essential biomolecules in multiple liver diseases.

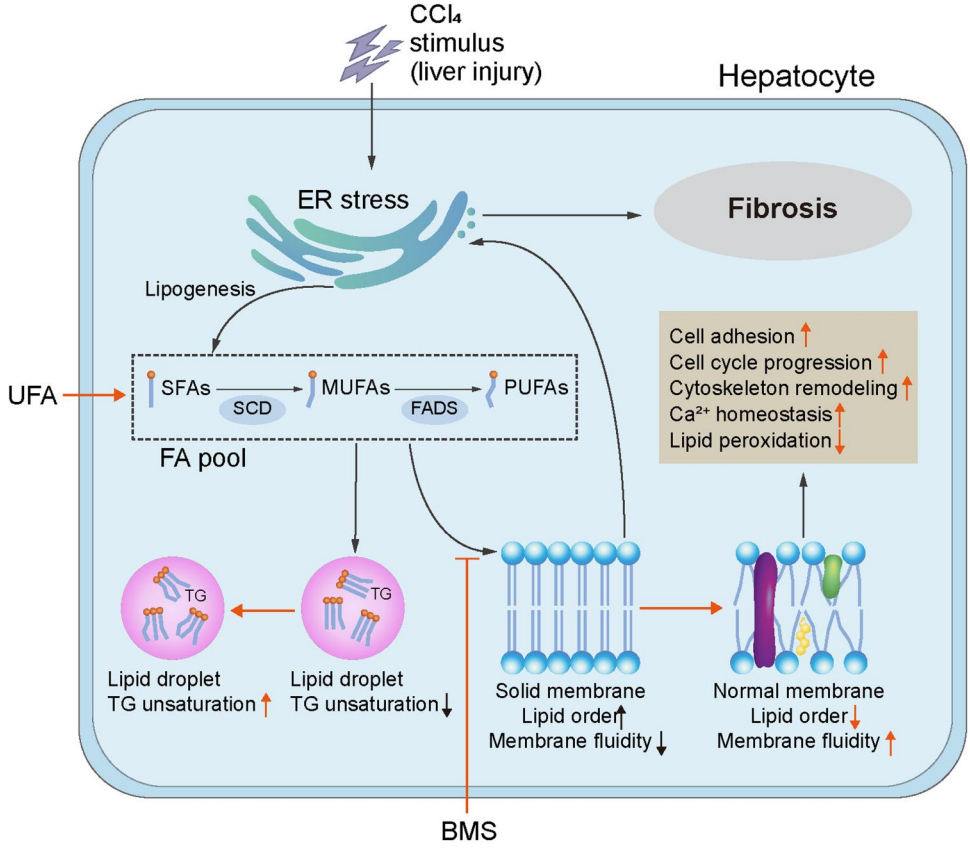

Fig. 8. Schematic of the proposed working model. CCl_4 stimulus on hepatocyte induces injury and ER stress, which further promotes lipogenesis, especially the initial product PAs. Owing to the up-regulated desaturation, some of the PAs are metabolized to UFAs, which, in turn, facilitate incorporation of PAs together into TGs and increase accumulation of LDs for prevention from lipotoxicity. Unfortunately, overwhelming PAs cannot be timely desaturated, which results in the decreased unsaturation degree of unsaturated TGs. Meanwhile, with the assistance of FABPs, excessive PAs that cannot be incorporated into LDs deliver to membranes, which further leads to the increased membrane lipid order and decreased membrane fluidity. Supplementation of UFAs can enhance incorporation of PAs into LDs, which increases lipid unsaturation degree, reduces membrane lipid order, increases membrane fluidity, and eventually rescues cells from toxicity and stress. Suppression of PA delivery to membranes by BMS can reduce membrane lipid order and increase membrane fluidity and, in the meanwhile, promotes LD accumulation via up-regulated TG synthesis and down-regulated lipolysis, which eventually ameliorates cellular processes.

Second, our study uncovers the role of altered lipid distribution in liver fibrosis. Although aberrant TG accumulation is commonly seen in liver diseases (*12*) and the lipid zonal location has been shown to be strongly related to histological features of nonalcoholic fatty liver disease (*16*, *51*), the zonal distribution of TG and its pathological significance in fibrotic liver remain unknown. Our imaging data revealed that TG accumulation was significantly increased in CV area, along with collagen fiber deposition, but almost absent in PV area. The rapid accumulation of TGs in CV area implies that CV may be the first area affected by fibrotic liver injury. These results indicate that molecular zonations of TGs and collagen fibers are closely associated with the development and progression of liver fibrosis, which has not been previously documented. The heterogeneous distribution of lipids and collagen fibers was also found in fibrotic livers in patients. Together, these findings suggest that the zonal patterns of lipids and collagen fibers could serve as valuable biomarkers for assessment of liver fibrosis progression.

Third, our study unravels the role of altered lipid composition in liver fibrosis. Although lipid accumulation has become a characteristic of liver fibrosis, whether and how the lipid composition changes during fibrosis is not known. CCl_4 stimulus could induce ER stress (*52*, *53*), which could further promote lipogenesis (*54*–*56*). As the initial product of lipogenesis, PA (C16:0) is desaturated and elongated to produce FA molecules with different unsaturation degrees and chain lengths (*57*). SFAs and UFAs are together esterified to TGs, in which FA chains are predominantly oleate (C18:1) and linoleate (C18:2), and then incorporated into LDs. In this work, we found a series of changes of lipid composition in the late-stage relative to the early-stage fibrosis, which are the increased amount of unsaturated TGs with decreased lipid unsaturation degree, the increased lipid peroxidation products, the decreased unsaturation degree of phospholipids, and the increased membrane lipid order. By integration of our imaging data with biochemical and molecular biology methods, we elucidate one of the possible mechanisms underlying these findings, as shown in Fig. 8. Specifically, the CCl_4 stimulus on hepatocyte induces injury and ER stress, which further promotes lipogenesis, especially the initial product PAs. Owing to the up-regulated desaturation, some of the PAs are metabolized to UFAs, which, in turn, facilitate incorporation of PAs together into TGs and increase accumulation of LDs for prevention from lipotoxicity. This explains why the amount of unsaturated TGs is increased during fibrosis. Unfortunately, in the late-stage fibrosis, overwhelming PAs cannot get desaturated in a timely manner, which may explain why the unsaturation degree of unsaturated TGs is decreased. Meanwhile, with the assistance of FABPs, excessive PAs that cannot be incorporated into LDs deliver to membranes. This may explain why, in fibrosis, the unsaturation degree of phospholipids is decreased, which further leads to the increased membrane lipid order and decreased membrane fluidity. Meanwhile, PUFAs also act as primary substrates for lipid peroxidation, which is a characteristic of oxidative stress in fibrosis. These dysregulated lipid and membrane homeostasis in turn promote ER stress and cell death, which creates a vicious circle. Of course, we cannot exclude other possibilities that may also contribute to the alteration of lipid composition in liver fibrosis, for instance, the relationship between hepatic insulin sensitivity and SFA fraction (*58*). Collectively, we elucidate the mechanism and significance of altered lipid composition in liver fibrosis.

Last, our study heralds the potential of regulating lipid homeostasis for liver fibrosis treatment. Liver fibrosis is a key factor for liver disease progression and hepatocellular carcinoma development. While many strategies have emerged to inhibit the development of liver fibrosis, including anti-inflammation, inhibition of hepatic stellate cell activation, and acceleration of extracellular matrix degradation, no approved therapy exists for liver fibrosis yet (*59*). Thus, there is an unmet need of novel therapies for liver fibrosis. Recently, reprogrammed FA metabolism has been targeted for liver fibrosis treatment, such as activation of FA oxidation and inhibition of acetyl-CoA carboxylase, rate-limiting step of de novo lipogenesis (*49*). In this work, we demonstrated two strategies for remodeling of lipid homeostasis to normalize cellular processes in injured hepatocyte (Fig. 8). First, supplementation of UFAs, especially OAs, can enhance incorporation of PAs into LDs, which increases lipid unsaturation degree, reduces membrane lipid order, increases membrane fluidity, and eventually rescues cells from toxicity and stress. Second, suppression of PA delivery to membranes by BMS, a small-molecule inhibitor for FABPs, can reduce membrane lipid order and increase membrane fluidity and, in the meanwhile, promotes LD accumulation via up-regulated TG synthesis and down-regulated lipolysis, which eventually ameliorates cellular processes. FABPs have become potential drug targets for multiple metabolic diseases (*60*). Together, this work offers potential therapeutic strategies to break the vicious circle between lipids and stress in liver fibrosis.

In summary, with the superior capability of quantitative chemical imaging, our multimodal imaging method revealed signature zonal pattern and dysregulated lipid composition of TGs in fibrotic liver, which have not been documented before. Integrative analyses further extend the understanding of dysregulated lipid homeostasis in liver fibrosis. Furthermore, this study may open new opportunities for liver fibrosis treatment by remodeling lipid homeostasis.

MATERIALS AND METHODS

Clinical sample

This study was approved by an institutional review board. The liver tissues were obtained from patients at transplantation for liver injury or cirrhosis in Beijing Tsinghua Changgung Hospital. The specimens were then snap-frozen in liquid nitrogen and stored in −80°C until further use.

Mouse model

All animal procedures were performed according to protocols approved by the Institutional Animal Care and Use Committee. Wild-type 6- to 8-week-old male adult C57BL/6J mice were obtained from Beijing Vital River Laboratory Animal Technology Company and were raised under standard pathogen-free conditions. All animal experiments were performed in accordance with the principles of care and use of laboratory animals. Intraperitoneal injection of a 1:1 mixture of CCl_4 with vegetable oil was administered twice a week at a dose of 0.5 μl/g for up to 12 weeks to induce liver fibrosis. The mice were euthanized on weeks 0, 2, 4, 6, 8, and 12 after treatment ($n = 3$ for each group). Liver tissues were harvested and snap-frozen in liquid nitrogen or embedded by paraffin until further use.

Tissue preparation

For each tissue specimen, pairs of neighboring slices were sectioned, with one slice (20 μm) remained unstained for multimodal NLO imaging and the other (5 μm) stained with H&E. A trained pathologist identified the CV and PV areas of each sample. The H&E slices were used to identify the same lobules for NLO imaging. Each unstained tissue slice was sandwiched by two glass coverslips for imaging.

Cell culture and treatment

HepaRG cells were cultured in RPMI 1640 (Gibco, 11875119), supplemented with 10% fetal bovine serum (Omega Scientific, FB-21), and 0.1% penicillin/streptomycin (Gibco, 15070063). Cell cultures were incubated in an incubator at 37°C with 5% CO_2.

PA, OA, EPA, and BMS were dissolved in dimethyl sulfoxide at designated concentrations before adding to cell culture media. After culturing for 1 day, growth medium was replaced with fresh medium containing FAs or inhibitor with indicated concentrations. Specifically, 400 μM PA, 200 μM OA, 50 μM EPA, and 50 μM BMS were used.

Chemical reagents

TS (T5016), TO (T7140), TL (T9517), PA-d_{31} (366897), OA (75090), EPA (44864), and anti-FABP1 antibody (HPA028275) were purchased from Sigma-Aldrich. Anti-malondialdehyde (GTX12835) was purchased from GeneTex. Anti-cytochrome P450 2E1 (ab28146), anti-GRP78 BiP antibody (ab21685), and anti–E-cadherin (ab40772) were purchased from Abcam. Anti–caspase-3 (A11021) was purchased from ABclonal. 4′,6-Diamidino-2-phenylindole (DAPI; BL105A) was purchased from Biosharp. CCl_4 (C805332) was purchased from Macklin. BMS-309403 (10010206) was purchased from Cayman Chemicals. Laurdan (D250) was purchased from Molecular Probes.

IHC and immunofluorescent staining

Tissues were fixed in 4% paraformaldehyde, embedded in paraffin, and then sectioned to 5-μm slices. For IHC, paraffin slices were rehydrated and incubated in antigen retrieval solution and blocking serum. The subsequent steps were performed using a Vector kit (Vector Laboratories) according to the manufacturer′s instructions. For immunofluorescent staining, the paraffin slices were permeabilized with 0.2% Triton X-100, blocked with 10% goat or donkey serum, and then incubated with primary antibodies at 4°C overnight. The slices were then incubated with secondary antibodies for 1 hour in the dark at room temperature, followed by DAPI incubation for nuclear staining. The immunofluorescent and IHC images were captured by an FV3000 (Olympus) microscope and a 3DHISTECH (Pannoramic MIDI) scanner, respectively.

Multimodal NLO microscopy

In our multimodal NLO microscopy setup (fig. S19), we used a picosecond pulse laser (picoEmerald S, Applied Physics & Electronics) with 80-MHz repetition rate and 2-ps pulse width. The laser has an integrated output for both the pump beam with tunable wavelength from 700 to 960 nm and the Stokes beam with fixed wavelength at 1031 nm, which are overlapped in space and time.

When performing SRS, the Stokes beam was modulated at ~20 MHz by an electronic optic modulator. The collinear pump and Stokes beams were coupled to a two-dimensional scanning galvanometer (GVS012-2D, Thorlabs) and then imported into an inverted microscope (IX73, Olympus). A 60× water-immersion objective lens (LUMPlanFL N, 1.0 numerical aperture, Olympus) was used to focus the light on the sample. Transmission of the forward-detected SRS signal was collected with another 60× water-immersion water objective (LUMPlanFL N, 1.0 numerical aperture, Olympus). A short-pass filter (ET980SP, Chroma) was used before a 10 mm by 10 mm large-area silicon photodiode (S3994-01, Hamamatsu) detector with 48 DC reversed bias voltage. The signal was then extracted by a lock-in amplifier (HF2LI, Zurich Instruments). The analog output representing the SRS signal was fed into a data acquisition card (PCIE-6363, National Instruments) and input to the computer to display the image on the LabVIEW 2018 software. To detect the vibrational bands of CH_2 (2850 cm^{-1}), ═C—H (3010 cm^{-1}), and C—D (2107 cm^{-1}), the wavelength of the pump beam was tuned to 796.8, 786.8, and 847 nm, respectively. The excitation power at the sample was ~20 mW for pump and ~90 mW for Stokes for all liver tissue samples.

As for hyperspectral SRS imaging, the Stokes beam was fixed at 1031 nm, and the pump beam was tuned to cover the CH vibrational region (2800 to 3050 cm^{-1}) with an interval of ~8 cm^{-1}. The SRS spectra of pure samples and the LDs of interest in liver tissue samples were then obtained on the basis of the hyperspectral SRS images.

On the same microscope, the pump beam was tuned to 796.8 nm, and the excitation power at the sample was ~40 mW for both SHG and TPEF imaging. A photomultiplier tube (H7422-40, Hamamatsu) was used to detect the backward SHG and TPEF signals through 395/25 nm (ET395/25, Chroma) and 520/40 nm (ET520/40, Chroma), respectively.

All images were obtained in 512 × 512 pixels with a dwell time of 8 μs per pixel. The large-scale images of tissue samples were recorded by a microscope motorized platform (H117, Prior). No photodamage to tissue was detected.

Spontaneous Raman spectra were acquired with a Raman microspectrometer (DR316B-LDC-DD, Andor), which was mounted to the side of the microscope. The pump beam was tuned to 707 nm for Raman spectra measurements. The excitation power at the sample was ~32 and ~20 mW for pure chemicals and liver tissue samples, respectively. Each Raman spectrum ranging from 600 to 3050 cm^{-1} was acquired in 20 s for pure chemicals and 60 s for liver tissue samples.

Data processing of SRS images

Quantification of total TGs, unsaturated TGs, and saturated TGs

As shown in fig. S5, LDs were selected according to their significantly higher signal intensities compared to other cellular compartments in the SRS image of CH_2 band at 2850 cm^{-1}, by using the ImageJ "Threshold" function. Then, the amount of LDs was quantified by the area fraction of LDs out of total image area. The LDs in liver fibrotic tissues were predominantly composed of TGs. Total TGs were extracted from the SRS image of CH_2 band at 2850 cm^{-1}, whereas unsaturated TGs were extracted from the SRS image of the ═C—H band at 3010 cm^{-1}. Subtracting the amount of unsaturated TGs from the amount of total TGs resulted in the amount of saturated TGs.

Quantification of lipid unsaturation degree

The lipid unsaturation degree here was designated as the number of C═C bands on each FA chain. The SRS images were first recorded from pure TS (C18:0), pure TO (C18:1), and pure TL (C18:2). Specifically, TS was used to represent saturated TGs, while TO and TL were used to represent unsaturated TGs. The unsaturation degrees of TO and TL are 1 and 2, respectively. We then performed SRS imaging of seven different molar ratios of TO/TL mixed emulsions, ranging from 0:10 to 10:0. As shown in Fig. 1C, the lipid unsaturation degree of unsaturated TGs was found to be linearly proportional with the SRS intensity ratio of the CH_2 band and the ═C─H band ($I_{=C-H}/I_{CH_2}$). Specifically, $I_{=C-H}/I_{CH_2}$= 0.2 × unsaturation degree + 0.1, where the intercept was set to weak the background signal from pure saturated TGs for linear fitting. Because of the complex tissue microenvironment, the relatively weak SRS signal from LDs at 3010 cm^{-1} was likely affected by the SRS signal from surrounding membranes. Thus, the original SRS image of the ═C─H band was first subtracted by the mean intensity of the surrounding signal for the liver tissue samples. Then, the lipid unsaturation degree of TGs in tissues was calculated on the basis of the established calibration curve shown in Fig. 1C.

The saturated TGs, unsaturated TGs, collagen fibers, and autofluorescent lipofuscin were pseudocolored in magenta, green, yellow, and cyan colors, respectively. All the large-scale image stitching was accomplished automatically by codes written in MATLAB R2018a.

Data processing of TPEF images

TPEF imaging of autofluorescent signals arose from both cellular structures and lipofuscins in liver tissues. Since lipofuscins emit much stronger autofluorescent signals compared to the surrounding cellular structures, we used an appropriate intensity threshold to segment the lipofuscins. The lipofuscins were colored in cyan color, whereas the surrounding structures were colored in gray color.

Mass spectrometry imaging

Sample preparation for DESI mass spectrometry imaging

Optimal cutting temperature (OCT)–embedded tissue sections were washed with ammonium formate/water to remove polyethylene glycol polymers (*61*). Tissues sections were submerged in cold (4°C) 150 mM NH_4HCO_2 for 3 s, and excess solution was removed by gently tapping the slides for 5 s. This process was repeated for multiple times (~5) until the OCT material was invisible.

Mass spectrometry imaging experiments

All data were acquired on Waters cyclic ion mobility mass spectrometer (Wilmslow, UK) equipped with a desorption electrospray ionization (DESI) source (Waters DESI XS, Wilmslow, UK). DESI geometry setup was optimized according to (*62*). Other instrument parameters were set as follows: solvent, 95:5 methanol-water with 0.1% formate acid/ammonium hydroxide for positive/negative mode; spray voltage, 4/4.5 kV for positive/negative mode; flow rate, 1.5 μl/min; nebulizing gas pressure, 5 bar (nitrogen); step size, 50 μm × 50 μm. Mass spectra were acquired across 50 to 1200 Th in both positive and negative modes.

Data processing

Raw imaging data files were first processed with HDImaging (Waters) to generate a text file containing pixel data of the 500 peaks of the highest intensity. The text file was then processed with an in-house MATLAB script for visualization of ion distributions (normalized to total ion current).

Membrane lipid order analysis of fibrotic liver tissues and live cells

Laurdan imaging was performed as previously described (*46*). Briefly, frozen tissues were stained with 25 μM Laurdan for 4 hour in phosphate-buffered saline at room temperature, and cells in glass-bottom dishes were stained with 5 μM Laurdan for 1 hour in serum-free medium at 37°C in a humidified incubator with 5% CO_2. Then, tissues and cells were imaged with multimodal NLO microscopy (excitation at 796.8 nm; emission at 440/40 and 520/40 nm). The pseudocolored GP images and hue-saturation-brightness (HSB) images were achieved using an ImageJ plug-in as described (*46*). HSB images that merged mean intensity and rainbow red-green-blue (RGB) color GP images were shown. GP values were quantified from GP images by ImageJ. Frequency of pixels with each GP value was plotted into histograms by Origin 2017.

RNA-seq transcriptomic analysis of fibrotic liver tissues

For the RNA-seq transcriptomic analysis of mouse liver fibrotic tissues, the RNA-seq data were downloaded from the National Center for Biotechnology Information (NCBI) GEO database with the accession IDs GSE214119, GSE207855, and GSE205540. The differentially expressed genes (DEGs) were identified as those with a fold change of more than 2 and an adjusted *P* value of less than 0.05. On the basis of the DEGs, GO biological process term enrichment analysis was carried out using the OmicShare tools (https://omicshare.com/tools).

RNA-seq transcriptomic analysis of cell samples

Total RNA was first extracted by TRIzol reagent (Invitrogen). Then RNA-seq experiments were performed by Novogene (Beijing, China). Sequencing libraries were generated using the NEBNext Ultra RNA Library Prep Kit for Illumina (New England Biolabs, USA) following the manufacturer′s recommendations. Independent libraries were constructed for triplicate samples for all assays and then were sequenced on an Illumina HiSeq platform. The DEGs were identified as those with a fold change of more than 2 and an adjusted *P* value of less than 0.05. All RNA-seq data related to Figs. 6 and 7 of this study have been deposited into NCBI GEO database (https://ncbi.nlm.nih.gov/geo/; accession ID: GSE220856).

Statistical analysis

Statistical analysis was performed using Origin 2017. The amount of collagen fiber and TG in mouse fibrotic liver tissues was shown as mean ± SD. The Student′s *t* test was used for comparisons of collagen fiber amount, TG amount, unsaturated TG proportion, and the lipid unsaturation degree in CV and PV areas. *P* value < 0.05 was considered statistically significant.

Supplementary Materials

This PDF file includes:

Figs. S1 to S19

Tables S1 to S6

View/request a protocol for this paper from *Bio-protocol*.

REFERENCES AND NOTES

1. E. Trefts, M. Gannon, D. H. Wasserman, The liver. *Curr. Biol.* **27**, R1147–R1151 (2017).
2. R. Manco, S. Itzkovitz, Liver zonation. *J. Hepatol.* **74**, 466–468 (2021).
3. K. Jungermann, T. Kietzmann, Zonation of parenchymal and nonparenchymal metabolism in liver. *Annu. Rev. Nutr.* **16**, 179–203 (1996).
4. V. Hernandez-Gea, S. L. Friedman, Pathogenesis of liver fibrosis. *Annu. Rev. Pathol.* **6**, 425–456 (2011).
5. T. Kisseleva, D. Brenner, Molecular and cellular mechanisms of liver fibrosis and its regression. *Nat. Rev. Gastroenterol. Hepatol.* **18**, 151–166 (2021).
6. W. Sun, S. Chang, D. C. Tai, N. Tan, G. Xiao, H. Tang, H. Yu, Nonlinear optical microscopy: Use of second harmonic generation and two-photon microscopy for automated quantitative liver fibrosis studies. *J. Biomed. Opt.* **13**, 064010 (2008).
7. Y. Wang, R. Vincent, J. Yang, A. Asgharpour, X. Liang, M. O. Idowu, M. J. Contos, K. Daitya, M. S. Siddiqui, F. Mirshahi, A. J. Sanyal, Dual-photon microscopy-based quantitation of fibrosis-related parameters (q-FP) to model disease progression in steatohepatitis. *Hepatology* **65**, 1891–1903 (2017).
8. F. Liu, G. B. Goh, D. Tiniakos, A. Wee, W. Q. Leow, J. M. Zhao, H. Y. Rao, X. X. Wang, Q. Wang, W. K. Wan, K. H. Lim, M. Romero-Gomez, S. Petta, E. Bugianesi, C. K. Tan, S. A. Harrison, Q. M. Anstee, P. J. Chang, L. Wei, qFIBS: An automated technique for quantitative evaluation of fibrosis, inflammation, ballooning, and steatosis in patients with nonalcoholic steatohepatitis. *Hepatology* **71**, 1953–1966 (2020).
9. Y. Yu, J. Wang, C. W. Ng, Y. Ma, S. Mo, E. L. S. Fong, J. Xing, Z. Song, Y. Xie, K. Si, A. Wee, R. E. Welsch, P. T. C. So, H. Yu, Deep learning enables automated scoring of liver fibrosis stages. *Sci. Rep.* **8**, 16016 (2018).
10. R. Dobie, J. R. Wilson-Kanamori, B. E. P. Henderson, J. R. Smith, K. P. Matchett, J. R. Portman, K. Wallenborg, S. Picelli, A. Zagorska, S. V. Pendem, T. E. Hudson, M. M. Wu, G. R. Budas, D. G. Breckenridge, E. M. Harrison, D. J. Mole, S. J. Wigmore, P. Ramachandran, C. P. Ponting, S. A. Teichmann, J. C. Marioni, N. C. Henderson, Single-cell transcriptomics uncovers zonation of function in the mesenchyme during liver fibrosis. *Cell Rep.* **29**, 1832–1847.e8 (2019).
11. A. Hall, C. Cotoi, T. V. Luong, J. Watkins, P. Bhathal, A. Quaglia, Collagen and elastic fibres in acute and chronic liver injury. *Sci. Rep.* **11**, 14569 (2021).
12. N. L. Gluchowski, M. Becuwe, T. C. Walther, R. V. Farese Jr., Lipid droplets and liver disease: From basic biology to clinical implications. *Nat. Rev. Gastroenterol. Hepatol.* **14**, 343–355 (2017).
13. R. J. Schulze, M. A. McNiven, Lipid droplet formation and lipophagy in fatty liver disease. *Semin. Liver Dis.* **39**, 283–290 (2019).
14. H. Wobser, C. Dorn, T. S. Weiss, T. Amann, C. Bollheimer, R. Buttner, J. Scholmerich, C. Hellerbrand, Lipid accumulation in hepatocytes induces fibrogenic activation of hepatic stellate cells. *Cell Res.* **19**, 996–1005 (2009).
15. J. Moon, E. Kong, J. Lee, J. Jung, E. Kim, S. B. Park, P. Kim, Intravital longitudinal imaging of hepatic lipid droplet accumulation in a murine model for nonalcoholic fatty liver disease. *Biomed. Opt. Express* **11**, 5132–5146 (2020).
16. Z. Hall, N. J. Bond, T. Ashmore, F. Sanders, Z. Ament, X. Wang, A. J. Murray, E. Bellafante, S. Virtue, A. Vidal-Puig, M. Allison, S. E. Davies, A. Koulman, M. Vacca, J. L. Griffin, Lipid zonation and phospholipid remodeling in nonalcoholic fatty liver disease. *Hepatology* **65**, 1165–1180 (2017).
17. C. Zhang, D. Zhang, J. X. Cheng, Coherent Raman scattering microscopy in biology and medicine. *Annu. Rev. Biomed. Eng.* **17**, 415–445 (2015).
18. J. X. Cheng, X. S. Xie, Vibrational spectroscopic imaging of living systems: An emerging platform for biology and medicine. *Science* **350**, eaaa8870 (2015).
19. S. Yue, J. X. Cheng, Deciphering single cell metabolism by coherent Raman scattering microscopy. *Curr. Opin. Chem. Biol.* **33**, 46–57 (2016).
20. Y. Shen, F. Hu, W. Min, Raman imaging of small biomolecules. *Annu. Rev. Biophys.* **48**, 347–369 (2019).
21. T. Chen, A. Yavuz, M. C. Wang, Dissecting lipid droplet biology with coherent Raman scattering microscopy. *J. Cell Sci.* **135**, jcs252353 (2022).
22. J.-X. Cheng, W. Min, Y. Ozeki, D. Polli, *Stimulated Raman Scattering Microscopy: Techniques and Applications* (Elsevier, 2021).
23. Y. M. Wu, H. C. Chen, W. T. Chang, J. W. Jhan, H. L. Lin, I. Liau, Quantitative assessment of hepatic fat of intact liver tissues with coherent anti-Stokes Raman scattering microscopy. *Anal. Chem.* **81**, 1496–1504 (2009).
24. J. Lin, F. Lu, W. Zheng, S. Xu, D. Tai, H. Yu, Z. Huang, Assessment of liver steatosis and fibrosis in rats using integrated coherent anti-Stokes Raman scattering and multiphoton imaging technique. *J. Biomed. Opt.* **16**, 116024 (2011).
25. M. Yarbakht, P. Pradhan, N. Kose-Vogel, H. Bae, S. Stengel, T. Meyer, M. Schmitt, A. Stallmach, J. Popp, T. W. Bocklitz, T. Bruns, Nonlinear multimodal imaging characteristics of early septic liver injury in a mouse model of peritonitis. *Anal. Chem.* **91**, 11116–11121 (2019).
26. C. W. Freudiger, W. Min, B. G. Saar, S. Lu, G. R. Holtom, C. He, J. C. Tsai, J. X. Kang, X. S. Xie, Label-free biomedical imaging with high sensitivity by stimulated Raman scattering microscopy. *Science* **322**, 1857–1861 (2008).
27. D. Fu, Y. Yu, A. Folick, E. Currie, R. V. Farese Jr., T. H. Tsai, X. S. Xie, M. C. Wang, In vivo metabolic fingerprinting of neutral lipids with hyperspectral stimulated Raman scattering microscopy. *J. Am. Chem. Soc.* **136**, 8820–8828 (2014).
28. P. Wang, B. Liu, D. Zhang, M. Y. Belew, H. A. Tissenbaum, J. X. Cheng, Imaging lipid metabolism in live *Caenorhabditis elegans* using fingerprint vibrations. *Angew. Chem. Int. Ed. Engl.* **53**, 11787–11792 (2014).
29. K. Bae, W. Zheng, K. Lin, S. W. Lim, Y. K. Chong, C. Tang, N. K. King, C. B. Ti Ang, Z. Huang, Epi-detected hyperspectral stimulated raman scattering microscopy for label-free molecular subtyping of glioblastomas. *Anal. Chem.* **90**, 10249–10255 (2018).
30. Y. Urasaki, C. Zhang, J. X. Cheng, T. T. Le, Quantitative assessment of liver steatosis and affected pathways with molecular imaging and proteomic profiling. *Sci. Rep.* **8**, 3606 (2018).
31. S. Yan, S. Cui, K. Ke, B. Zhao, X. Liu, S. Yue, P. Wang, Hyperspectral stimulated raman scattering microscopy unravels aberrant accumulation of saturated fat in human liver cancer. *Anal. Chem.* **90**, 6362–6366 (2018).
32. A. C. S. Talari, Z. Movasaghi, S. Rehman, I. U. Rehman, Raman spectroscopy of biological tissues. *Appl. Spectrosc. Rev.* **50**, 46–111 (2014).
33. S. Yue, J. Li, S. Y. Lee, H. J. Lee, T. Shao, B. Song, L. Cheng, T. A. Masterson, X. Liu, T. L. Ratliff, J. X. Cheng, Cholesteryl ester accumulation induced by PTEN loss and PI3K/AKT activation underlies human prostate cancer aggressiveness. *Cell Metab.* **19**, 393–406 (2014).
34. S. Yue, J. M. Cardenas-Mora, L. S. Chaboub, S. A. Lelievre, J. X. Cheng, Label-free analysis of breast tissue polarity by Raman imaging of lipid phase. *Biophys. J.* **102**, 1215–1223 (2012).
35. R. Pérez Tamayo, Is cirrhosis of the liver experimentally produced by CCl4 and adequate model of human cirrhosis? *Hepatology* **3**, 112–120 (1983).
36. P. Ramachandran, A. Pellicoro, M. A. Vernon, L. Boulter, R. L. Aucott, A. Ali, S. N. Hartland, V. K. Snowdon, A. Cappon, T. T. Gordon-Walker, M. J. Williams, D. R. Dunbar, J. R. Manning, N. van Rooijen, J. A. Fallowfield, S. J. Forbes, J. P. Iredale, Differential Ly-6C expression identifies the recruited macrophage phenotype, which orchestrates the regression of murine liver fibrosis. *Proc. Natl. Acad. Sci. U.S.A.* **109**, E3186–E3195 (2012).
37. P. Ramachandran, R. Dobie, J. R. Wilson-Kanamori, E. F. Dora, B. E. P. Henderson, N. T. Luu, J. R. Portman, K. P. Matchett, M. Brice, J. A. Marwick, R. S. Taylor, M. Efremova, R. Vento-Tormo, N. O. Carragher, T. J. Kendall, J. A. Fallowfield, E. M. Harrison, D. J. Mole, S. J. Wigmore, P. N. Newsome, C. J. Weston, J. P. Iredale, F. Tacke, J. W. Pollard, C. P. Ponting, J. C. Marioni, S. A. Teichmann, N. C. Henderson, Resolving the fibrotic niche of human liver cirrhosis at single-cell level. *Nature* **575**, 512–518 (2019).
38. Y. Shi, T. Yan, X. Lu, K. Li, Y. Nie, C. Jiao, H. Sun, T. Li, X. Li, D. Han, Phloridzin reveals new treatment strategies for liver fibrosis. *Pharmaceuticals (Basel)* **15**, 896 (2022).
39. E. Jarc, T. Petan, Lipid droplets and the management of cellular stress. *Yale J. Biol. Med.* **92**, 435–452 (2019).
40. J. Storch, A. E. Thumser, The fatty acid transport function of fatty acid-binding proteins. *Biochim. Biophys. Acta* **1486**, 28–44 (2000).
41. T. Hanhoff, C. Lücke, F. Spener, Insights into binding of fatty acids by fatty acid binding proteins. *Mol. Cell. Biochem.* **239**, 45–54 (2002).
42. G. van Meer, D. R. Voelker, G. W. Feigenson, Membrane lipids: Where they are and how they behave. *Nat. Rev. Mol. Cell Biol.* **9**, 112–124 (2008).
43. D. de Mendoza, M. Pilon, Control of membrane lipid homeostasis by lipid-bilayer associated sensors: A mechanism conserved from bacteria to humans. *Prog. Lipid Res.* **76**, 100996 (2019).
44. Y. Shen, Z. Zhao, L. Zhang, L. Shi, S. Shahriar, R. B. Chan, G. Di Paolo, W. Min, Metabolic activity induces membrane phase separation in endoplasmic reticulum. *Proc. Natl. Acad. Sci. U.S.A.* **114**, 13394–13399 (2017).
45. D. M. Owen, A. Magenau, A. Majumdar, K. Gaus, Imaging membrane lipid order in whole, living vertebrate organisms. *Biophys. J.* **99**, L7–L9 (2010).
46. D. M. Owen, C. Rentero, A. Magenau, A. Abu-Siniyeh, K. Gaus, Quantitative imaging of membrane lipid order in cells and organisms. *Nat. Protoc.* **7**, 24–35 (2011).
47. S. M. Lee, S. H. Lee, Y. Jung, Y. Lee, J. H. Yoon, J. Y. Choi, C. Y. Hwang, Y. H. Son, S. S. Park, G. S. Hwang, K. P. Lee, K. S. Kwon, FABP3-mediated membrane lipid saturation alters fluidity and induces ER stress in skeletal muscle with aging. *Nat. Commun.* **11**, 5661 (2020).
48. H. Ariyama, N. Kono, S. Matsuda, T. Inoue, H. Arai, Decrease in membrane phospholipid unsaturation induces unfolded protein response. *J. Biol. Chem.* **285**, 22027–22035 (2010).
49. S. Hwang, K. W. Chung, Targeting fatty acid metabolism for fibrotic disorders. *Arch. Pharm. Res.* **44**, 839–856 (2021).
50. J. Du, Y. Su, C. Qian, D. Yuan, K. Miao, D. Lee, A. H. C. Ng, R. S. Wijker, A. Ribas, R. D. Levine, J. R. Heath, L. Wei, Raman-guided subcellular pharmaco-metabolomics for metastatic melanoma cells. *Nat. Commun.* **11**, 4830 (2020).

51. H. Alamri, N. H. Patterson, E. Yang, P. Zoroquiain, A. Lazaris, P. Chaurand, P. Metrakos, Mapping the triglyceride distribution in NAFLD human liver by MALDI imaging mass spectrometry reveals molecular differences in micro and macro steatosis. *Anal. Bioanal. Chem.* **411**, 885–894 (2019).
52. A. Iracheta-Vellve, J. Petrasek, B. Gyongyosi, A. Satishchandran, P. Lowe, K. Kodys, D. Catalano, C. D. Calenda, E. A. Kurt-Jones, K. A. Fitzgerald, G. Szabo, Endoplasmic reticulum stress-induced hepatocellular death pathways mediate liver injury and fibrosis via stimulator of interferon genes. *J. Biol. Chem.* **291**, 26794–26805 (2016).
53. H. Xu, Q. Zhao, N. Song, Z. Yan, R. Lin, S. Wu, L. Jiang, S. Hong, J. Xie, H. Zhou, R. Wang, X. Jiang, AdipoR1/AdipoR2 dual agonist recovers nonalcoholic steatohepatitis and related fibrosis via endoplasmic reticulum-mitochondria axis. *Nat. Commun.* **11**, 5807 (2020).
54. A. Baiceanu, P. Mesdom, M. Lagouge, F. Foufelle, Endoplasmic reticulum proteostasis in hepatic steatosis. *Nat. Rev. Endocrinol.* **12**, 710–722 (2016).
55. J. Y. Kim, R. Garcia-Carbonell, S. Yamachika, P. Zhao, D. Dhar, R. Loomba, R. J. Kaufman, A. R. Saltiel, M. Karin, ER stress drives lipogenesis and steatohepatitis via caspase-2 activation of S1P. *Cell* **175**, 133–145.e15 (2018).
56. C. Liu, B. Zhou, M. Meng, W. Zhao, D. Wang, Y. Yuan, Y. Zheng, J. Qiu, Y. Li, G. Li, X. Xiong, H. Bian, H. Zhang, H. Wang, X. Ma, C. Hu, L. Xu, Y. Lu, FOXA3 induction under endoplasmic reticulum stress contributes to non-alcoholic fatty liver disease. *J. Hepatol.* **75**, 150–162 (2021).
57. F. Röhrig, A. Schulze, The multifaceted roles of fatty acid synthesis in cancer. *Nat. Rev. Cancer* **16**, 732–749 (2016).
58. K. H. M. Roumans, L. Lindeboom, P. Veeraiah, C. M. E. Remie, E. Phielix, B. Havekes, Y. M. H. Bruls, M. Brouwers, M. Stahlman, M. Alssema, H. P. F. Peters, R. de Mutsert, B. Staels, M. R. Taskinen, J. Boren, P. Schrauwen, V. B. Schrauwen-Hinderling, Hepatic saturated fatty acid fraction is associated with de novo lipogenesis and hepatic insulin resistance. *Nat. Commun.* **11**, 1891 (2020).
59. Z. Tan, H. Sun, T. Xue, C. Gan, H. Liu, Y. Xie, Y. Yao, T. Ye, Liver fibrosis: Therapeutic targets and advances in drug therapy. *Front. Cell Dev. Biol.* **9**, 730176 (2021).
60. M. Furuhashi, G. S. Hotamisligil, Fatty acid-binding proteins: Role in metabolic diseases and potential as drug targets. *Nat. Rev. Drug Discov.* **7**, 489–503 (2008).
61. J. X. M. Truong, X. Spotbeen, J. White, J. V. Swinnen, L. M. Butler, M. F. Snel, P. J. Trim, Removal of optimal cutting temperature (O.C.T.) compound from embedded tissue for MALDI imaging of lipids. *Anal. Bioanal. Chem.* **413**, 2695–2708 (2021).
62. J. Tillner, V. Wu, E. A. Jones, S. D. Pringle, T. Karancsi, A. Dannhorn, K. Veselkov, J. S. McKenzie, Z. Takats, Faster, more reproducible DESI-MS for biological tissue imaging. *J. Am. Soc. Mass Spectrom.* **28**, 2090–2098 (2017).

Acknowledgments

Funding: This work was supported by the National Natural Science Foundation of China (nos. 91959120 and 62027824 to S.Y., nos. 92168207 and 81730052 to Y.W., nos. 81930119 and 82090053 to J.D., and nos. 82090051 and 32000970 to J.L., Chinese Academy of Medical Sciences Innovation Fund for Medical Sciences (2019-I2M-5-056 to J.D.), Basic Research Program for Beijing-Tianjin-Hebei Coordination [no. 19JCZDJC65500(Z) to S.Y.], Fundamental Research Funds for the Central Universities (no. YWF-21-BJ-J-549 to S.Y.), National Key Research and Development Program of China (no. 2022YFA1103401 to Y.W.), Natural Science Foundation of Beijing (no. 7214306 to J.L.), Beijing Hospitals Authority Ascent Plan (no. DFL20190901 to Y.W.), Beijing Hospitals Authority Youth Programme (no. QML20200903 to J.L.), and Tsinghua Precision Medicine Foundation (no.2022TS013 to J.L.). **Author contributions:** H.J. conducted the NLO image acquisition, Raman spectrum acquisition, and data analysis. H.J. wrote the manuscript. J.L. and R.L performed the animal experiments. J.L. and Q.W. conducted histological staining. T.F., C.L., and X.C. developed a MATLAB script for image stitching. Z.Z., D.S., and W.Z. assisted with part of the data acquisition. Y.Q. and Z.O. conducted the mass spectrometry imaging and data analysis. J.D. contributed to conceptualization. S.Y. and Y.W. were responsible for experimental design and supervision. S.Y. and Y.W. wrote and edited the manuscript. All authors contributed to the study and critically reviewed the manuscript. **Competing interests:** The authors declare that they have no competing interests. **Data and materials availability:** All data needed to evaluate the conclusions in the paper are present in the paper and/or the Supplementary Materials.

Submitted 30 March 2022
Accepted 12 December 2022
Published 13 January 2023
10.1126/sciadv.abq2937